

Wave-in-deck loads and response of a TLP model in unidirectional regular waves

Nagi Abdussamie^a, Yuriy Drobyshevski^a, Roberto Ojeda^a, Giles Thomas^b, Walid Amin^a

^aNational Centre for Maritime Engineering and Hydrodynamics

Australian Maritime College, University of Tasmania, Launceston, TAS 7250, Australia

^bDepartment of Mechanical Engineering, University College London, UK

Abstract

Model tests of a moored tension leg platform (TLP) subjected to cyclonic conditions represented by deterministic regular waves were conducted with the aim of validating state-of-the-art two phase numerical simulations of wave-in-deck impact events. Tendon tension forces and localised slamming pressures at the deck underside were simultaneously measured using repeated runs. The computational fluid dynamics (CFD) simulations were based on the volume of fluid (VOF) method implemented in the commercial CFD code STAR-CCM+. The TLP's rigid body motions and the effect of tendons were simulated by means of an overset grid and massless spring lines, respectively. The global response and tendon tensions computed by the CFD code were found to be in good agreement with the measurements. The aft tendons were found to experience slackness following the deck impact in many wave cycles. CFD results showed that the downward component of the vertical wave-in-deck force was approximately synchronised with the minimum tendon tensions and evidently caused such slack situations. Although CFD simulations indicated that there was a strong interaction between water and air phases at the moment of impact, the air compressibility did not show a significant difference on the magnitude of impact pressures.

Keywords: tension leg platforms; wave-in-deck loads; dynamic response; numerical simulations.

Introduction

Loads generated by extreme wave-in-deck events are one of the most important causes of damage to fixed and floating offshore structures, especially in extreme storm conditions (Kaiser et al., 2009, Abdussamie et al., 2014a, Forristall, 2007, Scharnke and Hennig, 2015, Buchan et al., 1999, REUTERS, 2016). Offshore installations such as those located in the Australian North West Shelf (NWS), Gulf of Mexico and the North Sea are exposed to cyclones/hurricanes which can generate these severe wave events. For instance, Buchan et al. (1999) reported on the impact of tropical cyclone Olivia on Australia's NWS. The storm caused significant damage to oil and gas facilities in the region. Another example of this is the destruction of 126 offshore structures and the severe damage of 183 other structures during the period 2004 – 2005 due to the hurricanes Ivan, Katrina and Rita in the Gulf of Mexico (Kaiser et al., 2009). Most recently, in December 2015, living quarters of 50 workers of an offshore drilling rig in the North Sea were damaged when an enormous wave hit the accommodation block and left one person dead and two injured (REUTERS, 2016). Impairing the safety of life and/or damage to structure or equipment can have costly economic and safety implications. Consequently, there is a requirement by classification societies to ensure that an offshore facility can survive in extreme wave conditions (Lee et al., 2014, ABS, 2014, API, 2010, DNV, 2009). The slam events and the associated forces must be correctly and accurately accounted for in the design stage.

The current engineering knowledge required to accurately predict the magnitude and distribution of wave-in-deck loads and the resulting global response of a floating structures such tension leg platforms (TLPs) and semi-submersibles remains limited. This fact is reflected in the very limited number of papers reporting on model tests and numerical analyses of typical multi-column floaters currently available in the open literature. Johannessen et al. (2006) and Hennig et al. (2011) investigated the dynamic air gap, wave

loads and floating platform response under extreme wave conditions. Both investigations reported that a wave-in-deck event can lead to an additional extreme response mechanism and a step change in the extreme loading magnitude. It must be noted that complete and detailed results of these types of experiments are usually subjected to project confidentiality requirements and are therefore not available in the public domain.

Model tests are arguably the best approach for estimating wave-in-deck loads (Scharnke et al., 2014). However, this approach is costly, time-consuming and involves a number of drawbacks such as scaling effects. Alternatively, the use of computational fluid dynamics (CFD) based methods for calculating wave induced loads on offshore structures has been increasing. Commonly used commercial codes such as STAR-CCM+ and ANSYS FLUENT are available for modelling and solving wave-in-deck impact problems using the volume of fluid (VOF) method to capture free-surface hydrodynamic flows (CD-Adapco, 2012, Fluent, 2009). Recently, a robust overset grid technique has been developed to allow for numerical models with six degrees of freedom (6DOF) (Chen et al., 2008). Unlike traditional mesh techniques such as dynamic mesh, the mesh in the overset grid technique does not deform and thereby remeshing is not required. The technique can therefore be used for modelling large amplitude motions such as the case of the surge motion in TLPs. Nevertheless, any new CFD simulation technique can only be trusted by the industry if its results have been thoroughly validated against experimental data first.

There is a large body of work on CFD investigations of wave impact loads on fixed deck structures (Abdussamie et al., 2014b, Birknes-Berg and Johannessen, 2015, Iwanowski et al., 2014, Ren and Wang, 2004). However very little work on fixed with columns and floating structures has been reported to date. Buchner and Bunnik (2007) employed an improved VOF (iVOF) method implemented in ComFLOW for solving the dynamic response of the SNORRE-A TLP subjected to extreme regular waves. Rudman and Cleary (2013) employed

the Smoothed Particle Hydrodynamics (SPH) technique to simulate the fully non-linear dynamics of a large breaking wave hitting a TLP. These numerical studies (Buchner and Bunnik, 2007, Rudman and Cleary, 2013) were not validated against model tests. Wu et al. (2014) conducted a numerical study using STAR-CCM+ to investigate the air gap of a TLP under irregular extreme waves by applying the same input wave signal used in the model test. Each wave signal required 20 or more iterations in order to achieve a satisfactory match between measurements and numerical results. This implies that their proposed CFD technique is still too time expensive to be used for practical applications (Birknes-Berg and Johannessen, 2015).

The literature review discussed above showed that there are no detailed, combined numerical-experimental wave-in-deck investigations on floating offshore structures available for scientific research in the public domain. Therefore, the objective of this study is to investigate the problem in a systematic way by introducing both experimental and numerical procedures. The scope of the present investigation is to examine the global response of a conventional TLP at a model scale of 1:125 due to extreme wave events corresponding to a 10,000-year cyclonic condition. Regular wave tests were conducted in the Australian Maritime College (AMC) towing tank. Using data from repeated runs, uncertainty tests of wave elevations, tendon tensions, surge motion and slam pressures at the deck underside were performed. In addition, the commercial CFD code STAR-CCM+ was used to investigate the characteristics of unidirectional regular wave impact on the model. The overset grid technique was used to model rigid body motions. The TLP tendons were modelled using massless spring lines. The numerical results were then validated against the measurements acquired in model tests.

Experimental investigation

Experimental setup

The TLP model was divided into two parts namely a hull module (columns and pontoons) and a topside deck module. The TLP hull module was represented by four circular columns

and four square pontoons; the scaled model dimensions were based on the SNORRE-A TLP (Almeland et al., 1991). The main principles of the structure are given in Table 1. A square deck box of 608 mm \times 608 mm and 210 mm high was constructed (Figure 1). Previous studies examined the deck individually and the deck and hull as a combined structure (Abdussamie et al., 2016a, Abdussamie et al., 2016b). The operating scaled draft was maintained and the resulting static deck clearance, i.e., the vertical distance from the still-water level (SWL) to the deck underside, was 120 mm (15.0 m full scale), as given in Table 1. The 1:125 water depth does not represent the actual operational water depth of SNORRE-A, this was due to the limitations imposed by the maximum operational water depth of the towing tank of 1.5 m (Abdussamie et al., 2016a).

Table 1. Key principles for SNORRE-A TLP at full and model scales.

Parameter	Full scale	Tested model scale
Column diameter	25.00 m	200 mm
Pontoon size, height \times width	11.50 x 11.50 m	92 x 92 mm
Column spacing	76.00 m	608 mm
Column height	63.00 m	505 mm
Deck size, length \times breadth \times height	124.5 \times 92.0 \times 15.0 m	608 \times 608 \times 210 mm
Deck clearance, a_0	27.00 m	120 mm
Platform draft	38.125 m	305 mm
Displacement	101840 t	52.15 kg
Total mass	77640 t	39.75 kg
Initial pretension per leg, T_o	6055 t	3.10 kg
Number of tendons per leg, n	4	1
Total tendon length at zero offset, L_o	307 m	1195 mm
Axial stiffness per leg, nEA/L_o	2.42×10^8 N/m	15.80 N/mm
Riser tension	3320 t	1.70 kg
Centre of gravity, $C_g(x, y, z)$	n/a	(0.0, 0.0, 5.0) mm
Mass moment of inertia (I_{xx}, I_{yy}, I_{zz})	n/a	(5.23, 5.23, 5.63) kg.m ²
Water depth	310.00 m	1500 mm

Figure 1.

The rotation point of the tendons at the TLP model end was located at the column base. For that purpose a hinge was installed for each column at $z = -310$ mm, i.e., the model's keel

(Figure 2). The tendon anchor point was fixed at $z = -1470$ mm on the towing tank floor. One single stiff tendon for each leg was used at model scale in order to represent the mooring system of the SNORRE-A TLP (Table 1). The actual axial compliance of the four SNORRE-A TLP tendons was modelled using a custom stainless steel extension spring with the appropriate scaled stiffness. The light spring (0.06 kg) with a calibrated axial stiffness of approximately 15.8 N/mm was installed between a 3.2 mm stainless steel wire rope and an anchor base (Figure 2). For Leg#1 (up-wave tendon) and Leg#4 (down-wave tendon), the spring was connected to a waterproof load cell. The maximum total mass of each 1195 mm long tendon (wire rope + spring + load cell) was measured to be approximately 0.10 kg in air. The use of such an assembly implies that gravity and hydrodynamic loads acting on the tendon were neglected in model tests. The 30 mm \times 30 mm \times 30 mm anchor base block was 3D printed and connected to the tank floor using stainless steel studs such that it provided a strong fixture for the model. In order to adjust the initial pretension, each tendon was connected to a 1.2 mm stainless steel wire run through the anchor base block to an adjustable turnbuckle having short pitch threads and attached to the tank side.

Figure 2.

A series of model tests was conducted at the AMC towing tank which is 100 m long and 3.55 m wide and can be operated at a maximum water depth of 1.5 m. The TLP model was setup on the tank centreline with its initial centroid ($x = y = 0.0$) being located 15.0 m away from the wavemaker (Figure 3). Wave elevations around the TLP model were recorded using five wave probes. The location of each probe (denoted as WP) is presented in Table 2, being defined with respect to the origin point of the right-hand-rule local coordinate system shown in Figure 3.

Table 2. Location of wave probes used in the model tests with respect to the model's initial centroid.

Wave probe (WP)	Location (x, y) without the model (m)	Location (x, y) with the model (m)
1	(-10.0, 1.275)	(-10.0, 1.275)
2	(-5.0, 1.275)	(-5.0, 1.275)
3	(-1.0, 0.0)	(-1.0, 0.0)
4	(-0.404, 1.20)	(-0.304, 0.0) moving with the model
5	(0.0, 1.20)	(0.304, 0.0) moving with the model

Figure 3.

As illustrated in Figure 2, the model's surge motion was measured by a MagneRule magnetostrictive linear displacement transducer (MLDT). The up-wave and down-wave tendons were instrumented by two FUTEK submersible S-beam junior load cells (Model LSB210). Besides, the underside of the topside deck structure was instrumented with sixteen piezoresistive pressure transducers (denoted by PT#) distributed in xy plane in order to measure localised wave-in-deck slamming pressures (Figure 4). The model specifications of the different pressure transducers (approximately 4.0 mm in diameter) can be found in (Abdussamie et al., 2016a). A sampling frequency of 20 kHz was chosen for all channels in order to capture the short-duration slamming pressures (DNV, 2010).

Figure 4.

The two cyclonic sea states at the Australian NWS, 100-year and 10,000-year, were represented by several deterministic regular waves trains (Table 3). Eight test conditions that vary in wave steepness were investigated in order to provide an insight into the interaction between the TLP model and the oncoming waves. The input wave parameters for each wave are summarised in Table 4 where λ is the wavelength iteratively estimated from the dispersion relationship (DNV, 2010). The wave steepness ($S = H/\lambda$) indicates that all generated wave conditions were within non-breaking wave limits. At zero offset/set-down, test condition 3 and 8 had a crest height, η_c , approximated by the Stokes second order, exceeding the static deck clearance of 120 mm ($a = a_0 - \eta_c$). In order to obtain good experimental data and ensure repeatability and accuracy in the measurements of both global

and local wave impact loads, each test condition was repeated up to five times.

Table 3. Sea state selected for model tests.

Sea state	Full scale		Model scale (1:125)	
	H_s (m)	T_p (s)	H_s (mm)	T_p (s)
10,000-year	22.125	17.0	177	1.52
100-year	14.0	14.5	112	1.297

Table 4. Input wave parameters of wave conditions tested in towing tank.

Condition	H_{input} (mm)	T_{input} (s)	η_c (mm)	λ (m)	Sea state	H_{input}/H_s	S (-)	a (mm)
1	177	1.52	95.60	3.61	10,000-yr	1.00	0.049	24.4
2	200	1.52	109.10	3.61	10,000-yr	1.13	0.055	10.9
3	220	1.52	121.00	3.61	10,000-yr	1.24	0.061	-1.0
4	148	1.163	82.20	2.11	Arbitrary	-	0.070	37.8
5	201.6	1.163	115.90	2.11	Arbitrary	-	0.095	4.1
6	112	1.297	59.80	2.63	100-yr	1.00	0.043	60.2
7	168	1.297	92.50	2.63	100-yr	1.50	0.064	27.5
8	224	1.297	127.10	2.63	100-yr	2.00	0.085	-7.1

Uncertainty analyses of experimental data

In order to ascertain the uncertainty in the model test results, a single wave period associated with condition 2 ($H_{input} = 200$ mm, $T_{input} = 1.52$ s) is discussed below. Wave elevation measured by WP3 over four repeated runs and the resulting surge motion measured by the MLDT are shown in Figure 5, whilst the simultaneous wave elevations measured at the topside deck LE (WP4) and TE (WP5) are plotted in Figure 6. The tendon tensions measured in the up-wave tendon (Leg#1) and down-wave tendon (Leg#4) denoted by maximum tension (T_{max}) and minimum tension (T_{min}) are given in

Figure 7. By comparing the time history using four repeated runs, a good repeatability (low variability) can be appreciated for all measured parameters.

Figure 5.

Figure 6.

As a result of deck impact the model seems to experience a large offset and then decelerated to its neutral position, i.e., displacement ≈ 0.0 (Figure 5). Besides, the up-wave and down-wave tendons were both found to experience high frequency loadings (Figure 7). By referring

to Figure 8 which shows Fast Fourier Transform (FFT) results, a significant variability in loading magnitude was observed at frequency band of 4 – 5 Hz amongst the tested runs, particularly in Leg#1, which demonstrates the nonlinear effects of ringing loads (occurred at the heave natural period) and the dynamic response of the load cells used in the experiments.

Figure 7.

Figure 8.

In order to quantify the uncertainty associated with wave elevations and the resulting global impact loads and motions, the maximum (+) and minimum (-) values were extracted from the time history of WP3 and MLDT (Table 5), and WP4, WP5 and the submersible load cells (Table 6). The data variation was assessed by means of standard deviation (σ) and coefficient of variation ($CV = \sigma/\text{mean}$). The measured wave at WP3 had a mean wave height of 219.60 mm which is approximately 10% larger than the input wave height ($H_{\text{input}} = 200$ mm) used by the wavemaker. All peak values (+) demonstrated good repeatability with a small CV ($\leq 5\%$). The minima of the surge motion were found to have a large CV which can be attributed to the lower obtained mean value as the standard deviation was found to be minimal. While the maximum tension (T_{max}) was comparable in both legs, the minimum tension (T_{min}) in the down-wave tendon was found to be much lower than that measured in the up-wave tendon. It is worth mentioning that the down-wave tendons were found to be susceptible to slack situations (\approx zero tension) caused by a large suction force as evident from the trough amplitude (-) measured at WP5 (TE) which was found to be larger than that measured at WP4 (LE), see Table 6.

Table 5. Variation of measured wave elevations at WP3 and surge motion using four repeated runs.

Run	WP3 (mm)		Surge (mm)	
	(+)	(-)	(+)	(-)
1	134.60	-86.86	144.00	4.28
2	131.64	-83.82	145.90	4.34
3	139.43	-89.39	152.18	5.15
4	130.53	-82.14	154.14	7.14
Mean	134.05	-85.55	149.06	5.23
σ	3.98	3.22	4.87	1.34
CV	3%	4%	3%	26%

Table 6. Variation of measured wave elevations at WP4 and WP5 and tension in the up-wave tendon (Leg#1) and down-wave tendon (Leg#4) using four repeated runs.

Run#	WP4 (mm)		WP5 (mm)		up-wave tendon (N)		down-wave tendon (N)	
	(+)	(-)	(+)	(-)	T_{max}	T_{min}	T_{max}	T_{min}
1	124.82	-86.77	120.46	-109.54	68.17	21.63	66.32	4.38
2	113.20	-89.00	121.64	-111.66	71.81	22.90	71.49	4.86
3	120.15	-91.06	123.62	-105.06	75.00	21.61	68.42	6.71
4	119.92	-86.82	121.52	-118.81	76.21	23.04	74.28	4.79
Mean	119.52	-88.41	121.81	-111.27	72.80	22.30	70.13	5.19
σ	4.78	2.05	1.32	5.73	3.60	0.78	3.49	1.04
CV	4%	2%	1%	5%	5%	4%	5%	20%

The wave-in-deck slam pressures around the forward and aft columns associated with the wave event ($H_{meas.} = 219.60$ mm, $T = 1.52$ s) are presented in Figure 9 and Figure 10, respectively. The pressure signal can typically be idealised by an impulse-like shape with a peak value (slam/impact pressure) followed by a slowly-varying phase. High frequency components were observed in the pressure signals of PT#3 (5.0 Hz and 385 Hz) and PT#14 (5.0 Hz and 485 Hz), located near the deck side edges, which can be attributed to the vertical vibration (≈ 5.0 Hz) experienced by the model during wave impact. The topic of hydro-elastic effects on localised wave-in-deck pressure measurements requires a further investigation.

Figure 9.

Figure 10.

The wave height and the corresponding impact pressures associated in each test run are summarised in Table 7. Using pairwise comparisons between wave height and impact pressures, there was no evidence of a correlation between the two parameters. For instance, in run 4 wave height of 212.67 mm (the lowest wave height) caused the largest impact pressure at PT#14 and PT#15.

Table 7. Variation of measured wave height at WP3 and impact pressures around the forward and aft columns using four repeated runs.

Run#	H (mm)	Forward column (kPa)			Aft column (kPa)		
	WP3	PT#1	PT#2	PT#3	PT#14	PT#15	PT#16
1	221.46	0.75	0.56	1.16	1.45	1.23	1.49
2	215.47	1.00	0.67	1.02	2.95	3.84	1.78
3	228.83	1.24	1.29	1.81	3.13	3.17	1.68
4	212.67	0.65	0.74	1.11	3.96	5.05	1.27
Mean	219.60	0.91	0.82	1.28	2.88	3.32	1.55
σ	6.20	0.23	0.28	0.31	0.91	1.39	0.19
CV	3%	25%	35%	24%	31%	42%	13%

The pressure distribution along the deck underside was presented using boxplots such that the variation among the different runs could be examined. The maximum and minimum values, the first quartile (the 25th percentile) and third quartile (the 75th percentile), Q1 and Q3, as well as the median pressure values, measured in multiple runs were combined into a single plot. The square symbol (▪) represents the mean value of peak pressures measured by a transducer in different runs (Figure 11). By referring to Table 7 a small variation in the measured wave elevation/wave height (CV = 3%) may lead to a very large variation in the magnitude of the impact pressure of up to 42% at PT#15. Such a finding highlights that the magnitude of slam pressure is very variable and its variability seems to be affected by the transducer location: whether near side edges, around the columns or in the middle of the deck underside. This reveals the necessity of conducting experiments repeated over multiple runs in order to obtain a reliable mean value of slam pressure which can be used for numerical validation purposes.

Figure 11.

Numerical investigation

The commercial Navier-Stokes CFD code STAR-CCM+ (Release 10) developed by CD-adapco was used for simulating the physics of the wave-in-deck problem. Since the CFD results were validated against model test results at a small scale, laminar flow was assumed for all numerical simulations. In this paper, based on isothermal and laminar flow assumptions, a system of partial differential equations governing the conservation of mass and momentum of a fluid was solved numerically using the finite volume method (Versteeg and Malalasekera, 2007).

The VOF model implemented in STAR-CCM+ was used for capturing the interface between two immiscible fluids, herein water and air phases. This implies that the trapped air involved in the wave-in-deck problem was accounted for. Both phases were modelled as an incompressible fluid, unless otherwise stated. The physical properties of water and air were expressed as a volume of fraction of each fluid during solving process. Further theoretical details of the numerical method can be found in the STAR-CCM+ user guide (CD-Adapco, 2012).

In the present numerical study, two different computational domains were created namely: a wave generation domain and a wave-structure interaction domain. In the second domain, an overset mesh was used to allow for 6DOF motions of the TLP model. The CFD analyses were conducted as per the following procedure:

- 1- Wave generation (similar to the wave calibration conducted in model tests) – a numerical wave tank (NWT) or wave generation domain was created without the TLP model being present in order to investigate wave quality generated against theoretical and measured wave elevations at different locations along the tank.

- 2- Wave-structure interaction (similar to the wave impact tests conducted in towing tank) – the TLP model was setup in the domain using overset mesh and subjected to unidirectional regular waves tested in step 1.

Wave generation domain discretisation

A 3D trimmed mesh with 1 cell layer into the y-direction was generated to investigate the numerical quality of the generated waves. The numerical wave tank used was 22 m long (approximately 6 wavelengths), 0.1 m wide and 2.0 m deep. It was divided into three identical zones (Figure 12) in x-direction, 2λ long each where λ is the maximum wave length tested ($\lambda = 3.61$ m). In order to minimise reflected waves from far-field boundaries, which can corrupt the numerical solution, the upstream and downstream boundaries were set at $x = 0$ and $x = 6\lambda$, respectively. Wave damping was applied over the last 2λ “damping zone” before the downstream boundary. The method proposed by Choi and Yoon (2009) is implemented into STAR-CCM+ for damping the vertical motion of the free surface.

The mesh domain was divided into several parts with different levels of mesh refinement (Table 8). Previous work by the authors (Abdussamie et al., 2014a, Abdussamie et al., 2014b) has identified that approximately 20 – 30 cells per wave height and 80 cells per wavelength were essential for the accurate prediction of wave propagation in the lower and upper free surface parts.

Figure 12.

Table 8. Relative mesh size to the base cell size of 0.2 m used for numerical wave tank during wave generation tests.

Part	Dimensions: Length × Width × Depth (m)	Relative size (%)		
		dx	dy	dz
Water	$22 \times 0.10 \times 1.35$	100	100	100
Air	$22 \times 0.10 \times 0.30$	100	100	100
Free surface	$22 \times 0.10 \times 0.35$	12.5	100	3.125
Total cell count	112,420			

Wave-structure interaction domain discretisation

The dynamic floating body interaction (DFBI) model implemented in STAR-CCM+ is capable of computing the 6DOF motions of a rigid body (CD-Adapco, 2012). In this investigation, unidirectional waves and the longitudinal symmetry plane allowed the model to be free in only 3DOF motions, namely surge, heave and pitch.

Two regions, a background region and an overset region, with two different coordinate systems were defined as illustrated in Figure 13. The overset region, which includes the TLP body, moves with the body over a static background region. Similarly to the NWT used to investigate the wave trains, the upstream and downstream boundaries were placed far enough away from the TLP's centroid (3λ) so that boundary effects on the flow could be minimised.

The global coordinate system $OXYZ$ of the background region was set to coincide with the right handed-coordinated system used in the model test and during the numerical wave generation simulations; with the xy -plane being on the SWL, the z -axis positive upward, and the origin at the left corner of the tank. The flow field and excitation forces and moments acting on the model were first solved in the global coordinate system. The obtained forces and moments were then transferred to the TLP body coordinate system located at its centre of mass at $x = 10.8$ m, $y = 0.0$ and $z = 1.505$ m.

Figure 13.

In order to interpolate forces and moments an overset mesh interface must be created between background and overset regions. A specific overset boundary condition was defined on the overset grids to allow for the flow interactions between the two regions. It is recommended that cells should be of comparable size in the overlapping zone (CD-Adapco, 2012). 3D trimmed mesh was used for both background and overset regions so that the free surface could be captured with a high accuracy. When generating the overset mesh, particular attention should be given to

1. Minimising errors in the interpolating variables between the overset and background meshes. It is recommended that the same order of magnitude of grid density, in the overlapping zone of the two, is employed.
2. The grid must be finer around the model and the free surface zone to capture relevant free surface details.

Table 9. Domain size for the background and overset regions and overlapping zone.

Dimension	Background region		TLP model		Overset region		Overlapping zone	
	Start	End	Start	End	Start	End	Start	End
Length, x (m)	0.0	22.0	10.396	11.204	10.296	11.304	10.196	11.404
Width, y (m)	0.0	1.775	0.0	0.404	0.0	0.604	0.0	0.504
Depth, z (m)	0.0	2.0	1.195	1.83	1.095	1.93	1.0	2.0

In order to fulfil these requirements a number of volumetric controls were setup including overlap volumetric control, free surface volumetric control and the TLP volumetric control (overset region), as detailed in Table 10. Figure 14 shows the distribution of trimmed cells near the TLP model.

In addition to gravity, flow-induced forces and moments due to shear and pressure terms affect body motions. Besides, couplings using spring lines were used to model the platform's tendons. Each tendon was modelled by a spring line with axial stiffness of 15.8 N/mm. The fairlead point was located at $z = 1195$ mm (column base), and the anchor point was fixed at $z = 0.0$ (tank floor). In order to specify the initial pretension, the relaxation length of each spring line was given as 1193 mm (2 mm elongation or equivalently $T_0 = 31.6$ N).

Table 10. Mesh size details in the background and overset regions.

Region	Base cell size	Part	Relative size (%)			Cell count
			dx	dy	dz	
Background	0.2 m	Water	100	100	100	743,700
		Air	100	100	100	
		Free surface	12.5	100	3.125	
		Overlapping	12.5	12.5	3.125	
Overset	0.1 m	Water	100	100	100	1.26×10^6
		Air	100	100	100	
		Free surface	25	100	6.25	
		Overlapping	25	25	6.25	
		Total				2.00×10^6

Figure 14.

Boundary and initial conditions

In order to model the desired wave characteristics, an incoming wave with appropriate height and wave period was specified at the inflow domain boundary ($x = 0.0$) shown on the left side of the diagram presented in Figure 12. At this boundary of the domain a velocity inlet condition was specified, where the velocity field and volume fraction of water and air were defined using the Stokes fifth order wave theory (Fenton, 1985). Hydrostatic pressure boundary condition was assigned at the top of the tank and its end the right side, i.e., the outflow boundary. No-slip boundary condition was used on the tank bottom ($z = 0$), tank side ($y = 1.775$ m) and the TLP model boundary surfaces. Whilst the other side of domain ($y = 0$) was set with a symmetry boundary condition. At time = 0.0, the wave field was initialised such that the wave profile was fully developed in “wave propagation” zone; from $x = 0$ to $x = 2\lambda$. This minimised the time required for incoming waves to reach $x = 10.8$ m (model’s centroid) in the wave-structure interaction simulations. A TLP model responds before being hit by waves and therefore the model was released 50 time steps after the solution starts (CD-Adapco, 2012). As the body is assumed to be rigid, elastic deformations effects were not considered.

Solution settings

The following solution parameters were found to be important to achieve good wave impact simulations: time step and the effect of damping zone (wave reflection). It was found that time step 0.001 s, 5 iterations per time step are adequate to maintain optimal HRIC-solution (Abdussamie et al., 2014b). It should be noted that STAR-CCM+ automatically changes the scheme used for transport volume fraction based upon upper and lower limits of Courant number used. Pure HRIC scheme is used when the local Courant number is below the lower

limit (0.5), whereas a pure first-order upwind scheme is automatically activated for Courant number higher than the upper limit (1.0). For intermediate limits, both schemes are blended (CD-Adapco, 2012).

The second-order discretisation of unsteady terms in momentum equations and HRIC scheme for the solution of the volume fraction equations was adopted in all simulations. The pressure-velocity coupling was performed by the SIMPLE (Semi-Implicit Method for Pressure Linked Equations) algorithm. Second order discretisation for convective terms of VOF model. Under-relaxation factors (URF) which are important for stability and convergence speed were used to reduce changes between iterations (Table 11). These settings were selected as a reasonable compromise between accuracy and computational time.

Table 11. Under-relaxation factors (URF) used in numerical simulations.

Equation	URF
Pressure correction	0.4
Velocity	0.9
Volume fraction	0.9

Prediction of wave-in-deck slam pressures

In order to capture slam pressure distribution at the deck underside, different levels of mesh refinement were investigated as summarised in Table 12. Fine surface mesh was applied to the entire underside of the topside deck (Figure 15). The diameter of transducer tip ($D_{\text{trans.}} \approx 4$ mm) was divided into a number of 2D (surface) cells. The level of mesh refinement was increased by a factor of 2 such that the transducer diameter covered 1.28 cells in level 1 and 5.12 in level 3 (Table 12). The local mesh refinement led to dramatically increase in the total cell count.

Table 12. Levels of local mesh refinement at the deck underside relative to the base cell size of overset region (0.10 m).

Level	Relative size (%)	Absolute size (mm)	$D_{\text{trans.}}/\text{absolute size (-)}$	Total cell count
1	3.12500	3.12500	1.28	2.00×10^6
2	1.56250	1.56250	2.56	2.37×10^6
3	0.78125	0.78125	5.12	4.10×10^6

Figure 15.

Assessment of CFD results

Wave quality

Several line probes were defined along the numerical domain to monitor the elevation magnitude of the waves propagating in the positive x -direction at $x = 5.8$ m (representing WP2), $x = 7.2$ m (end of wave propagation zone), $x = 9.8$ m (representing WP3), $x = 10.8$ m (representing WP5) and $x = 21.75$ m (inside wave damping zone). The accuracy of the CFD wave elevations was assessed on the basis of the input wave height. It is worth mentioning that wave period computed were found to be exactly same of the input one. However, as the wave propagates along the domain, similar to model tests, its crest height decays thereby underestimating the input wave height. Figure 16 presents the computed wave height averaged over several wave cycles associated with a simulation time of 20.0 s. Wave probes located in the area of interest, $x = 9.8$ m and $x = 10.8$ m, were found to be within 93% – 97% of the input wave height indicating good accuracy and deemed acceptable.

The efficiency of the damping zone was assessed by monitoring the time history of wave elevation at $x = 5.75\lambda$ or 0.25λ from the downstream boundary. In addition, the wave elevation along the domain at volume fraction of water = 0.5 was obtained at different instances of time (Figure 17). It should be noted that it is difficult to simulate waves with zero transport losses numerically due to relaxed spatial and temporal discretisation (Abdussamie et al., 2014b, Saripilli et al., 2014). Also, there is a tendency of NWT to build a phase difference of numerical wave with theoretical/measured wave which is generally noticed far away from the inlet boundary condition (Figure 17).

Figure 16.

Figure 17.

Mesh density

The maximum wave-in-deck slam pressure caused by the steepest wave condition (condition 5: $H_{\text{input}} = 201.6$ mm, $T_{\text{input}} = 1.163$ s) was utilised for sensitivity analyses due to local mesh density on the deck underside (Table 12). By referring to Figure 18 and using the time history of a single wave period out of seven impact events, the effect of mesh density was noticeable when results of level 2 (fine mesh) and level 3 (finer mesh) were compared with those of level 1 (reference mesh). These tests were conducted with air phase being incompressible and a time step of 0.001 s. When level 1 was taken as the reference mesh level; there was an increase in the peak pressure (maximum pressure) of approximately 20% using level 2 and 47% using level 3 which indicates that finer mesh may be necessary. However, the use of level 3 for local mesh refinement had an inconsistent effect on the maximum computed impact pressure indicating that the impact pressure is extremely localised phenomenon (Lee et al., 2014).

Figure 18.

Air compressibility

The effect of air compressibility was tested by comparing results of the maximum wave-in-deck pressure obtained using incompressible air phase with those performed using compressible air. Both numerical tests were conducted using mesh level 3 for condition 5 discussed above ($H_{\text{input}} = 201.6$ mm, $T_{\text{input}} = 1.163$ s). As seen in Figure 19, the air compressibility had an inconsistent effect on the slam pressure within the tested time frame. The use of incompressible air rather resulted in a smoother pressure signal than that produced by a compressible fluid.

Figure 19.

Comparison of experimental and CFD results

The first step was to conduct a numerical decay tests in STAR-CCM+ in order to obtain the damped natural periods of the combined TLP-mooring system. Using still-water simulations, the model was initialised by prescribed values (initial translational or angular velocity of 0.3 m/s) along the DOF of interest and then released to move freely. Table 13 summarises the results of these decay tests in the surge, heave and pitch degrees of freedom. As an example, Figure 20 shows time traces of surge decay system and the corresponding FFT results. Good agreement was achieved between the CFD and model tests, although damping ratios differed which can be attributed to the far-field boundary effects as the domain length was shorter than the physical tank.

Table 13. Damped natural periods of the TLP model obtained by model tests and CFD.

Motion	Experiment (s)	CFD (s)	CFD/Experiment (-)
Surge	5.660	5.61	0.99
Heave	0.225	0.21	0.93
Pitch	0.222	0.21	0.95

Figure 20.

Results of global response

Time histories of surge motion and tendon tensions for test conditions 2 and 3 are shown in Figure 21 and Figure 22, respectively. The predicted surge motion and tendon tensions by CFD were found to be in good agreement with the experimental results. Apart from the first impact, which caused by the transient start-up condition of wavemaker in model tests, the magnitude of surge motion and tension in both legs were well predicted by CFD simulations. With the assumption of zero pitch rotational motion, the platform set-down (Z) was estimated from the time history of the measured surge motion, $X(t)$, as $Z(t) = L_o - \sqrt{(L_o^2 - X^2)}$ (Demirbilek, 1990), $L_o = 1195$ mm. The estimated set-down was compared with the heave motion predicted by CFD (Figure 23). Good agreement was achieved between the estimated

and computed platform set-down for both conditions 2 and 3 indicating that the contribution of pitch motion in the magnitude of set-down was minimal.

Figure 21.

Figure 22.

Figure 23.

The maximum and minimum tensions in the up-wave and down-wave tendons are summarised in Table 14 for all conditions. Figure 24 shows the maximum surge amplitude (in positive x -direction) and the maximum and minimum tensions as a function of wave steepness (S). For condition 5 ($S = 0.095$) and condition 8 ($S = 0.085$) CFD solutions were found to over predict the minimum tension in the up-wave tendon. Such a discrepancy can be attributed to the sensitivity of load cells to zero/negative force as well as to the nonlinear response of spring line being different in CFD compared to the model tests. Furthermore, the initial pretension used in CFD models was set as constant ($T_o = 31.6$ N). This was not the case in the experimental model tests, where the measured initial pretension was found to vary and be sensitive to the initial condition for each individual test run. As seen in Table 15, the measured leg pretension was found to be within 91% – 115% of the computed leg pretension.

Table 14. Summary of maximum and minimum tensions in the up-wave and down-wave tendons for all conditions.

Condition	S (-)	up-wave tendon (N)				down-wave tendon (N)			
		T_{max}		T_{min}		T_{max}		T_{min}	
		CFD	Exp.	CFD	Exp.	CFD	Exp.	CFD	Exp.
1	0.049	36.39	37.97	27.19	25.72	39.13	42.40	19.48	19.00
2	0.055	38.05	40.44	26.09	23.24	41.19	44.04	16.35	11.65
3	0.061	42.33	42.80	22.40	22.85	44.77	45.89	10.44	9.60
4	0.07	37.06	41.30	26.73	31.04	71.61	79.20	39.13	47.85
5	0.095	57.90	63.23	1.27	9.54	61.50	67.16	0.00	0.00
6	0.043	32.88	36.57	28.80	30.76	37.01	48.39	35.50	41.85
7	0.064	36.20	41.33	27.27	28.35	39.91	49.71	18.03	13.08
8	0.085	67.07	73.17	1.89	9.78	70.07	83.54	0.00	0.00

Figure 24.Table 15: Measured leg pretension (T_o) and its ratio to the leg pretension using in CFD models ($T_o = 31.60$ N).

Condition	H_{input} (mm)	T_{input} (s)	S (-)	up-wave tendon		down-wave tendon	
				T_o (N)	Ratio (-)	T_o (N)	Ratio (-)
1	177.00	1.52	0.049	30.13	0.95	30.94	0.98
2	200.00	1.52	0.055	30.19	0.96	31.34	0.99
3	220.00	1.52	0.061	28.76	0.91	29.65	0.94
4	148.00	1.163	0.070	35.71	1.13	36.49	1.15
5	201.60	1.163	0.095	34.53	1.09	35.47	1.12
6	112.00	1.297	0.043	32.50	1.03	33.29	1.05
7	168.00	1.297	0.064	32.93	1.04	33.57	1.06
8	224.00	1.297	0.085	34.91	1.10	35.59	1.13

Wave-in-deck impact events

During model experiments the wave-in-deck impact events were identified through pressure measurements and using high speed cameras. It was observed that trapped waves between the forward and aft columns seem to be heightened due to wave upwelling and diffraction and hence caused local impacts at the deck underside. The minimum dynamic air gap due to the estimated platform set-down (Z) was given as $a_n = a_0 - (\eta_{meas.} - Z)$. Table 14 summarises the estimated values of a_n compared with those obtained at zero offset/set-down using input wave parameters ($a = a_0 - \eta_c$). The platform surge motion and set-down resulted in additional wave-in-deck impact events including conditions 1, 2 and 5.

Table 16. Effect of platform set-down on the dynamic air gap.

Condition	Input parameters			Measured and estimated parameters (averaged)			
	S (-)	η_c (mm)	a (mm)	X (mm)	$\eta_{meas.}$ (mm)	Z (mm)	a_n (mm)
1	0.049	95.60	24.40	47.97	117.72	-0.96	1.32
2	0.055	109.10	10.90	98.94	122.18	-4.10	-6.28
3	0.061	121.00	-1.00	115.20	143.42	-5.57	-28.99
4	0.070	82.20	37.80	140.47	96.25	-8.28	15.47
5	0.095	115.90	4.10	100.05	115.01	-4.20	0.79
6	0.043	59.80	60.20	80.05	81.26	-2.68	36.06
7	0.064	92.50	27.50	154.37	106.13	-10.01	3.86
8	0.085	127.10	-7.10	134.27	116.58	-7.57	-4.15

CFD models enabled for isolating the wave impact force components acting on the topside deck only (wave-in-deck forces) from the total hydrodynamic wave force being impacting on the TLP model. In most cases, the magnitude of the horizontal wave-in-deck forces (F_x) was insignificant, whilst the vertical wave-in-deck forces (F_z) were found to largely affect the global response of the TLP model. The dynamic tensions (T_0 was subtracted from the time history) in the up-wave and down-wave tendons were analysed along with F_z time history. Figure 25 shows CFD results of F_z time history associated with conditions 3, 5 and 8. Tendon slack situations were denoted by a dash line (force = -31.60 N). The aft tendons were found to experience slackness following the deck impact in many wave cycles. The downward component of F_z which was found to be approximately synchronised with the minimum tendon tensions evidently caused such slack situations.

Figure 25.

Time history of a single wave-in-deck impact event associated with condition 5 ($H_{\text{input}} = 201.6$ mm, $T_{\text{input}} = 1.163$ s) is presented in Figure 26. During this time history (time = 5.0 s – 6.5 s) four phases were defined as follows:

- Phase I (platform response: time = 5.0 s – 5.5 s) – it preceded the wave impact on the deck underside, the variation in tension could be caused by wave impact on the forward columns (including overtopping) and/or the ringing response associated with the previous deck impact. At this phase $F_z = 0.0$.
- Phase II (water entry: time = 5.5 s – 5.655 s) – two deck slams were identified: the first was at time = 5.534 s ($F_z = 50.77$ N) and the second occurred at time = 5.60 s ($F_z = 35.89$ N). The second slam was shorter than the first one.

- Phase III (water exit: time = 5.655 s – 6.0 s) – water detached from the deck underside started at time = 5.655 s, F_z was minimum ($F_z = -28.37$ N) and slackness occurred in the down-wave tendon. The phase completed at time = 6.0 s.
- Phase IV (platform response: time = 6.0 s – 6.5 s) – $F_z = 0.0$ and ringing response were pronounced in both tendons.

Qualitative comparisons between the experimental and numerical results were made in Figure 27 by showing the interaction between a large wave and the TLP model using snapshots at different time frames for condition 5.

Figure 26.

Figure 27.

The CFD simulations of wave-in-deck pressures were conducted using mesh level 3 and compressible air. The single wave-in-deck impact event discussed above for condition 5 ($H_{input} = 201.6$ mm, $T_{input} = 1.163$ s) was selected for further analyses. The maximum pressure caused by the wave impact throughout the deck underside was captured at each time step as shown in Figure 28. The pressure signal is denoted by four peaks (a) – (d). The first slam obtained in F_z (Figure 26) was found to coincide in the time interval between (a) and (b), whereas the second slam occurred in the time interval between (c) and (d). Figure 29 shows snapshots of pressure contours at the deck underside corresponding to the different time instances (a) – (d) where half of the deck underside and columns# 1 and 3 are only shown. The magnitude of impact pressure caused the first slam (a – b) was smaller but acting on larger area than that caused the second slam (c – d). This finding demonstrates the global and local effects of extreme wave impact event such that the global response of a TLP could be affected even by small slam pressure if the subject area of its deck underside was large. On the other hand, large slam pressures acting on small areas of its deck underside could result local damage, in particular around the aft columns (in the case of unidirectional waves).

By analysing the volume fraction of water during these time instances, the surface area subjected to wave slams contained a mixture of air and water (the water content was not 100%, i.e., water volume fraction $\neq 1.0$). For instance, at time instance (d), the area around the aft column experienced a maximum pressure of approximately 4885 Pa with a volume fraction of water was found to be almost 65% (35% air). This highlights the effectiveness of use two-phase numerical models for predicting wave-in-deck impact pressures.

Figure 28.

Figure 29.

As the area around the aft column was found to experience large slam pressures, a comparison of impact pressure at a discrete point representing the central location of pressure transducer PT#16 was made (Figure 30). As previously discussed, pressure measurements due to wave impact at discrete points were found to be extremely variable. Another complexity of model tests lies in the effect that regular waves often fail to reach the steady state and hence the wave-in-deck slam pressures vary in time and space. On the other hand, regular waves generated by CFD models demonstrated improved stability. CFD predictions of maximum pressure were found to favourably agree to the maximum pressure measured over repeated runs.

Figure 30.

Conclusions

Experimental and CFD investigations of a moored tension leg platform (TLP) subjected to cyclonic regular wave conditions were conducted to examine the global response and wave-in-deck impact problems. Based on the findings reported in this paper, the following conclusions could be drawn:

- Uncertainty analyses of data collected over 4 – 5 repeated runs demonstrated that the global loads and motions associated to extreme wave events affecting a TLP can be measured experimentally with low variability.
- The overset grid technique implemented in STAR-CCM+ was found to be capable of modelling large amplitude surge motions with an adequate numerical stability within the tested time frame for all simulated cases.
- The model's motions and tendon tensions predicted by CFD were found to be in good agreement with the measurements except for the initial transient periods caused by the start-up condition of the wavemaker.
- The aft tendons were found to experience slackness following the deck impact in many wave cycles. CFD results showed that the downward component of the vertical wave-in-deck force was approximately synchronised with the minimum tendon tensions and evidently caused such slack situations.
- Challenges remain in the measurements and computations of wave slamming pressures. Variability of the pressure measurements was found to be high; it is recommended to run at least five runs per each test to obtain a reliable pressure value.
- The leg pretension measured in model tests were found to be too sensitive to the initial conditions and varied amongst test runs. Another complexity of the model tests lies in the effect that regular waves often fail to reach the steady state and hence the wave-in-deck slam pressures vary in time and space. On the other hand, regular waves generated by CFD models demonstrated improved stability. Using the exact measured wave height and the tendon pretension would improve CFD results.
- Although CFD simulations showed that there was a strong water-air interaction at the moment of impact, the variation of air compressibility values did not generate a significant difference in the magnitude of the computed impact pressures. CFD

predictions of maximum pressure were found to favourably agree to the measured one provided that the pressure measurement is obtained over repeated runs.

The present numerical study using regular wave conditions validated against model tests could serve as a benchmark validation case for further numerical studies aimed at predicting wave-in-deck loading due to, e.g., combined waves with current and/or wind.

Acknowledgement

The authors acknowledge the assistance from the Australian Maritime College towing tank staff in the set up and execution of the model tests.

References

- Abdussamie, N., Amin, W., Ojeda, R., Thomas, G. & Drobyshevski, Y. Vertical Wave-in-Deck Loading and Pressure Distribution on Fixed Horizontal Decks of Offshore Platforms. Proceedings of the 24th International Offshore and Polar Engineering, 2014a Busan, South Korea. International Society of Offshore and Polar Engineers.
- Abdussamie, N., Ojeda, R., Amin, W., Thomas, G. & Drobyshevski, Y. Prediction of Wave-in-Deck Loads on Offshore Structures Using Cfd. the 19th Australasian Fluid Mechanics Conference, 2014b Melbourne, Australia. AFMS.
- Abdussamie, N., Ojeda, R., Drobyshevski, Y., Thomas, G. & Amin, W. 2016a. Experimental Investigation of Extreme Wave Impacts on a Rigid TLP Model in Cyclonic Conditions - "Accepted in-Press". *Ships and Offshore Structures*.
- Abdussamie, N., Ojeda, R., Drobyshevski, Y., Thomas, G. & Amin, W. 2016b. Measurements of Global and Local Effects of Wave Impact on a Fixed Platform Deck - "Accepted in-Press". *the Proceedings of the Institution of Mechanical Engineers, Part M: Journal of Engineers for the Maritime Environment*.
- ABS 2014. Rules for Building and Classing: Floating Production Installation. Houston, USA: American Bureau of Shipping, ABS.
- Almeland, I., Gaul, T., Pettersen, D. & Vogel, H. Snorre TLP Configuration and Analysis Technology. Proceedings of Offshore Technology Conference, 1991 Houston, USA. Offshore Technology Conference.
- API 2010. Planning, Designing, and Constructing Tension Leg Platforms: API Recommended Practice 2T Third Edition. USA: American Petroleum Institute, API.
- Birknes-Berg, J. & Johannessen, T. Methods for Establishing Governing Deck Impact Loads in Irregular Waves. The ASME 2015 34th Int. Conf. on Ocean, Offshore and Arctic Eng., OMAE2015, 2015 St. John's, Newfoundland, Canada. ASME.
- Buchan, S., Black, P. & Cohen, R. The Impact of Tropical Cyclone Olivia on Australia's Northwest Shelf. Proceedings of Offshore Technology Conference, 1999 Houston, USA. Offshore Technology Conference.
- Buchner, B. & Bunnik, T. Extreme Wave Effects on Deepwater Floating Structures. Offshore Technology Conference, 2007 Houston, Texas.
- CD-Adapco 2012. User Guide - STAR-CCM+ Version 7.04. CD-Adapco.
- Chen, H.-C., Lee, S.-K. & Seah, A. K. 2008. Overset Grid CFD Applications for Challenging Offshore Hydrodynamic Problems. *ABS Technical Paper*.
- Choi, J. & Yoon, S. B. 2009. Numerical Simulations Using Momentum Source Wave-Maker Applied to Rans Equation Model. *Coastal Engineering*, 56, 1043-1060.

- Demirbilek, Z. 1990. Design Formulae for Offset, Set Down and Tether Loads of a Tension Leg Platform (TLP). *Ocean engineering*, 17, 517-523.
- DNV 2009. Offshore Standard Det Norske Veritas: Structural Design of Tlps (LRFD Method). Høvik, Norway: Det Norske Veritas, DNV.
- DNV 2010. Recommended Practice DNV-RP-C205: Environmental Conditions and Environmental Loads. Høvik, Norway: Det Norske Veritas, DNV.
- Fenton, J. D. 1985. A Fifth-Order Stokes Theory for Steady Waves. *Journal of Waterway, Port, Coastal, and Ocean Engineering*, 111, 216-234.
- Fluent, A. 2009. Ansys Fluent 12.0 User Guide. ANSYS Inc.
- Forristall, G. Z. Wave Crest Heights and Deck Damage in Hurricanes Ivan, Katrina, and Rita. Offshore Technology Conference, 2007. Offshore Technology Conference.
- Hennig, J., Scharnke, J., Buchner, B. & van den Berg, J. Extreme Load-Response Mechanisms of a Tension Leg Platform Due to Larger Wave Crests: Some Results of the ‘Crest’ JIP. ASME 2011 30th International Conference on Ocean, Offshore and Arctic Engineering, 2011. American Society of Mechanical Engineers, 855-864.
- Iwanowski, B., Vestbostad, T. & Lefranc, M. Wave-in-Deck Load on a Jacket Platform, CFD Calculations Compared with Experiments. The ASME 33rd Int. Conf. on Ocean, Offshore and Arctic Eng., OMAE, 2014 San Francisco, CA, USA. ASME.
- Johannessen, T., Haver, S., Bunnik, T. & Buchner, B. 2006. Extreme Wave Effects on Deep Water TLPs Lessons Learned from the Snorre a Model Tests. *Proc. Deep Offshore Technology 2006*, 28-30.
- Kaiser, M. J., Yu, Y. & Jablonowski, C. J. 2009. Modeling Lost Production from Destroyed Platforms in the 2004–2005 Gulf of Mexico Hurricane Seasons. *Energy*, 34, 1156-1171.
- Lee, S.-K., Yu, K. & Huang, S. C. Cfd Study of Air-Gap and Wave Impact Load on Semisubmersible under Hurricane Conditions. The ASME 33rd Int. Conf. on Ocean, Offshore and Arctic Eng., OMAE, 2014 San Francisco, CA, USA. ASME.
- Ren, B. & Wang, Y. 2004. Numerical Simulation of Random Wave Slamming on Structures in the Splash Zone. *Ocean engineering*, 31, 547-560.
- REUTERS. 2016. *North Sea Storm Forces Oil Platform Evacuations, Output Shutdown* [Online]. Available: <http://www.reuters.com/article/us-weather-northsea-idUSKBN0UE00R20151231>.
- Rudman, M. & Cleary, P. W. 2013. Rogue Wave Impact on a Tension Leg Platform: The Effect of Wave Incidence Angle and Mooring Line Tension. *Ocean Engineering*, 61, 123-138.
- Saripilli, J. R., Joga, R. K., Dhavalikar, S. & Kar, A. R. Simulation of Numerical Wave Tanks for Generating Irregular Waves and Forward Speed Effects. The Twenty-fourth International Ocean and Polar Engineering Conference, 2014. International Society of Offshore and Polar Engineers.
- Scharnke, J. & Hennig, J. Vertical Wave Impact Loading on a Fixed Platform Deck. Proceedings of the ASME 2015 34th International Conference on Ocean, Offshore and Arctic Engineering, OMAE2015, 2015 St. John's, Newfoundland, Canada. American Society of Mechanical Engineers.
- Scharnke, J., Vestbostad, T., Wilde, J. d. & Haver, S. K. Wave-in-Deck Impact Load Measurements on a Fixed Platform Deck. Proceedings of the ASME 33rd International Conference on Ocean, Offshore and Arctic Engineering, OMAE, 2014 San Francisco, CA, USA. American Society of Mechanical Engineers.
- Versteeg, H. K. & Malalasekera, W. 2007. *An Introduction to Computational Fluid Dynamics: The Finite Volume Method*, Prentice Hall.
- Wu, G., Jang, H., Kim, J. W., Ma, W., Wu, M.-C. & O’Sullivan, J. Benchmark of CFD Modeling of TLP Free Motion in Extreme Wave Event. ASME 2014 33rd International Conference on Ocean, Offshore and Arctic Engineering, 2014. American Society of Mechanical Engineers, V002T08A086-V002T08A086.



Figure 1. Photograph showing the TLP model prior to model tests.

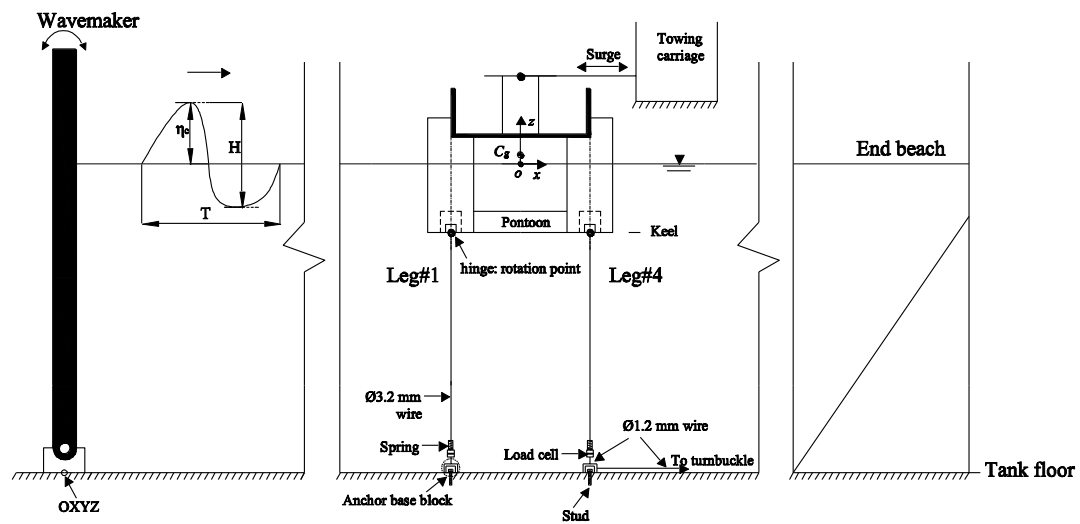


Figure 2. Profile view showing sketch definition of wave and the model setup at the AMC towing tank [not to scale]. The adjustment of pretension for each leg was performed through a turnbuckle connected to the tank side.

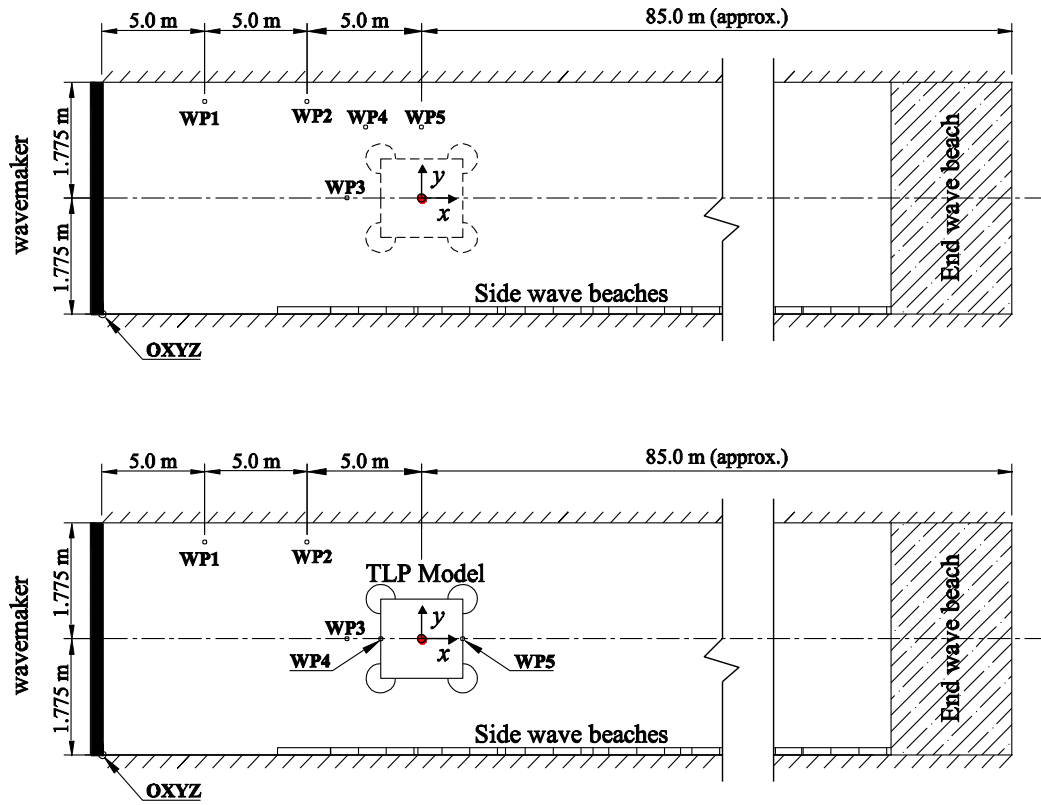


Figure 3. Plan view of the AMC towing tank showing the distribution of wave probes (WP): during wave calibration (top); during wave impact tests with the TLP model in-place (bottom) [not to scale].

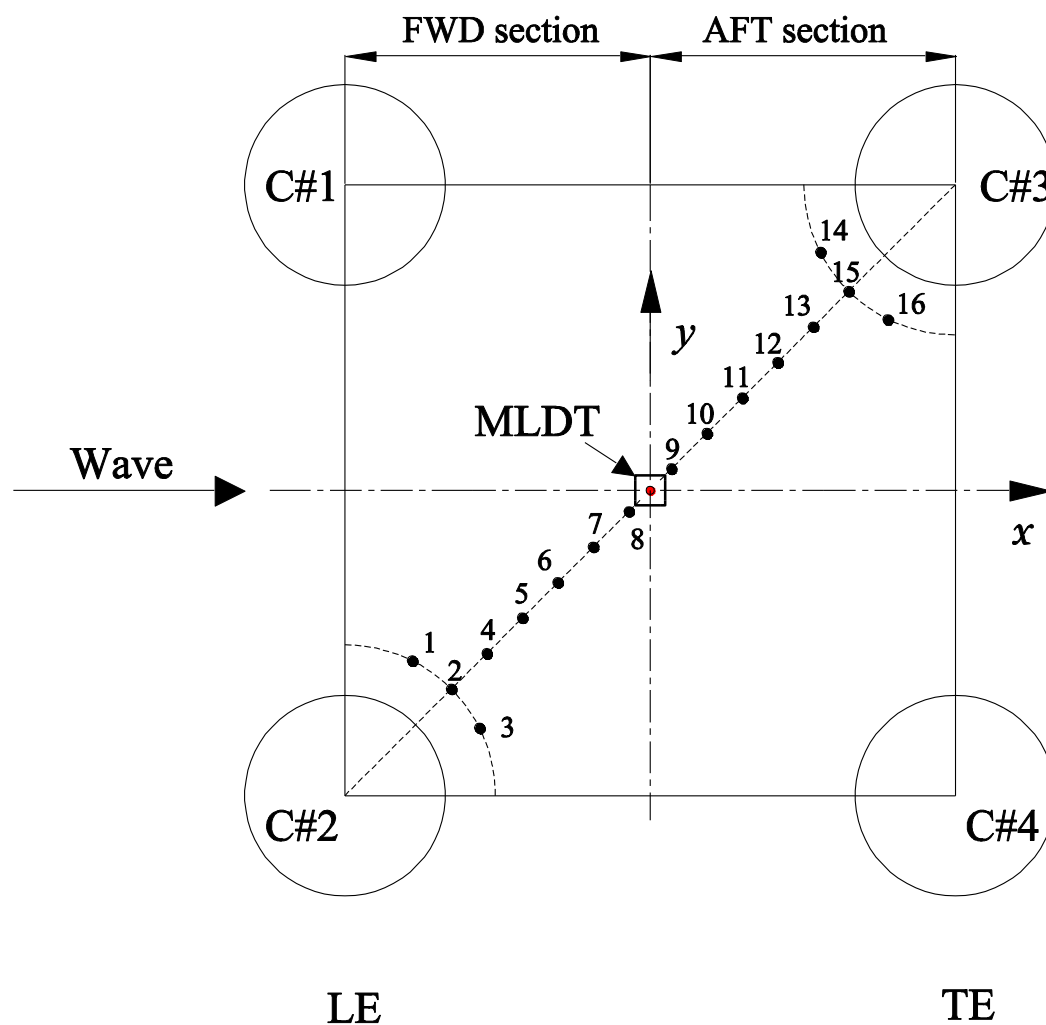


Figure 4. Plan view of the deck underside showing the distribution of pressure transducers (PT).

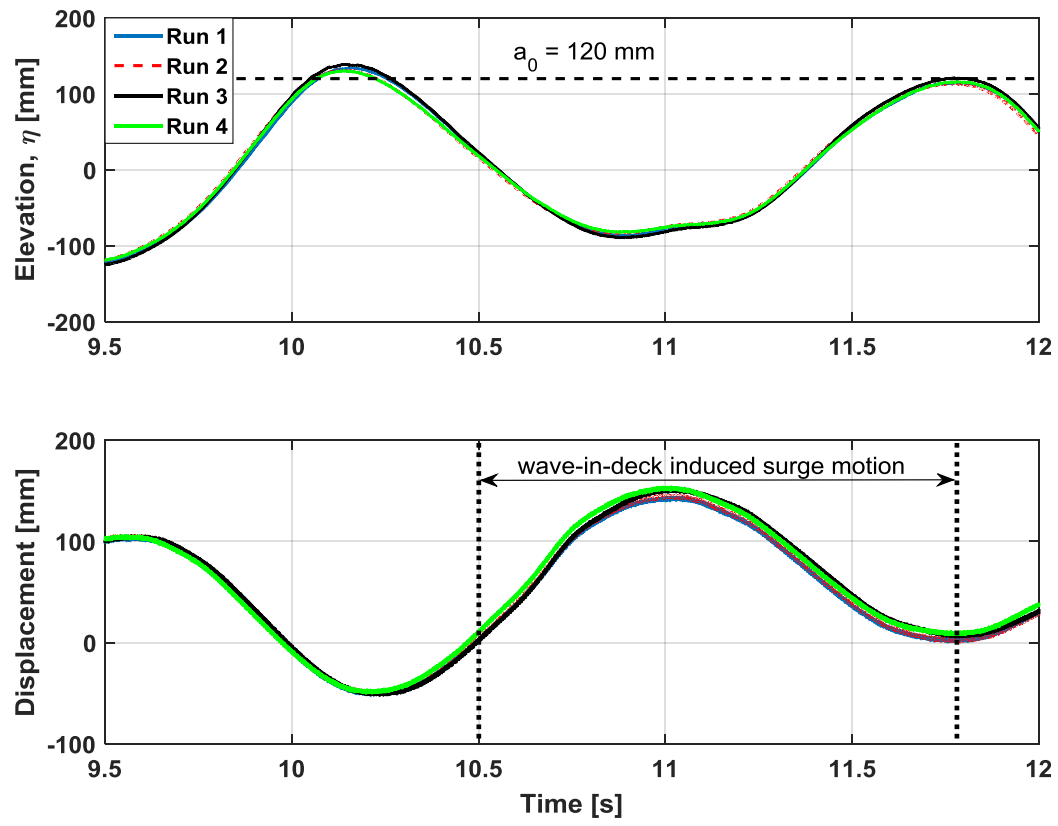


Figure 5. Time history of measured wave elevation of a single wave for condition 2 ($H_{\text{input}} = 200$ mm, $T_{\text{input}} = 1.52$ s) using four repeated runs: wave probe WP3 (top); surge motion (bottom).

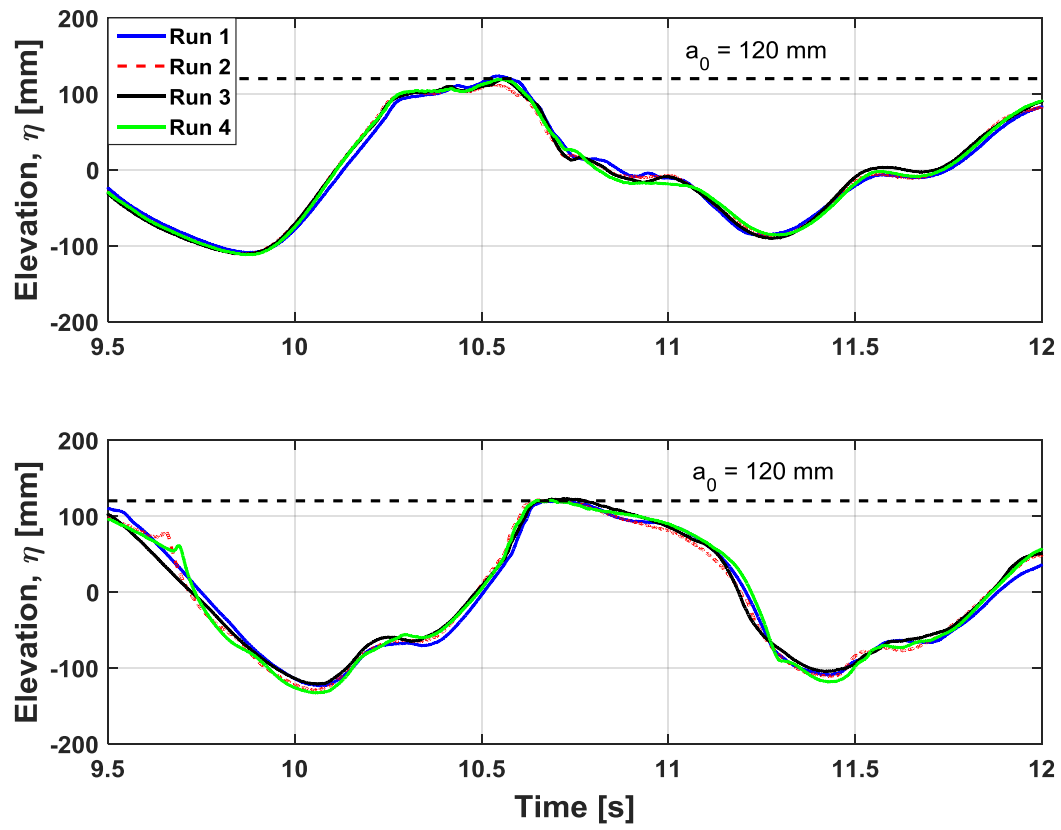


Figure 6. Time history of measured wave elevation of a single wave for condition 2 ($H_{\text{input}} = 200$ mm, $T_{\text{input}} = 1.52$ s) using four repeated runs: wave probe WP4 at LE (top); wave probe WP5 at TE (bottom).

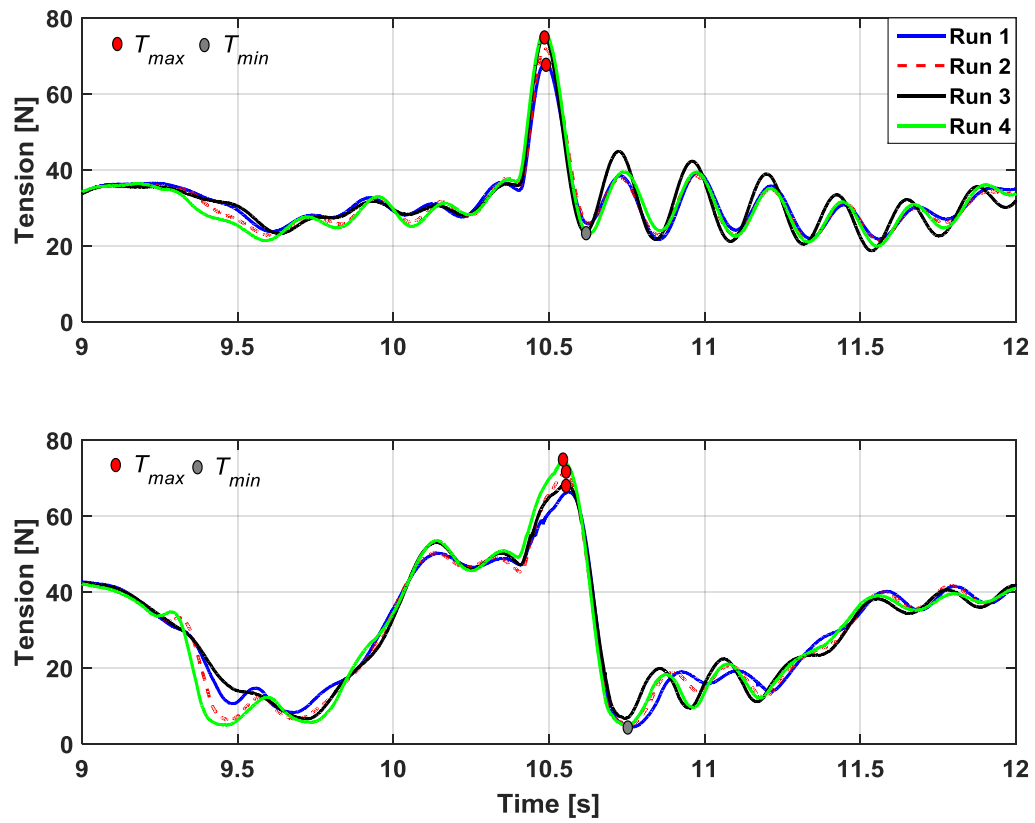


Figure 7. Time history of measured tension using four repeated runs ($H_{input} = 200$ mm, $T_{input} = 1.52$ s): up-wave tendon (top); down-wave tendon (bottom).

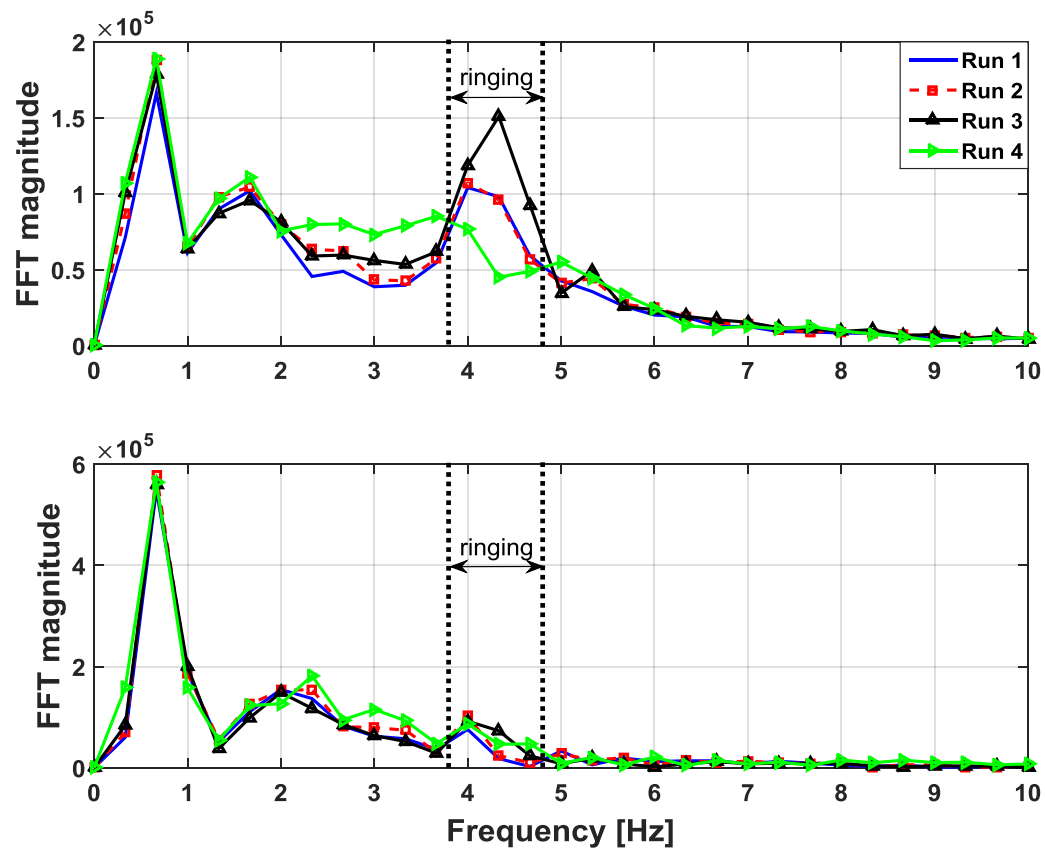


Figure 8. FFT results of tendon tensions using four repeated runs corresponding to the time history shown in Figure 7 for condition 2 ($H_{input} = 200$ mm, $T_{input} = 1.52$ s): up-wave tendon (top); down-wave tendon (bottom).

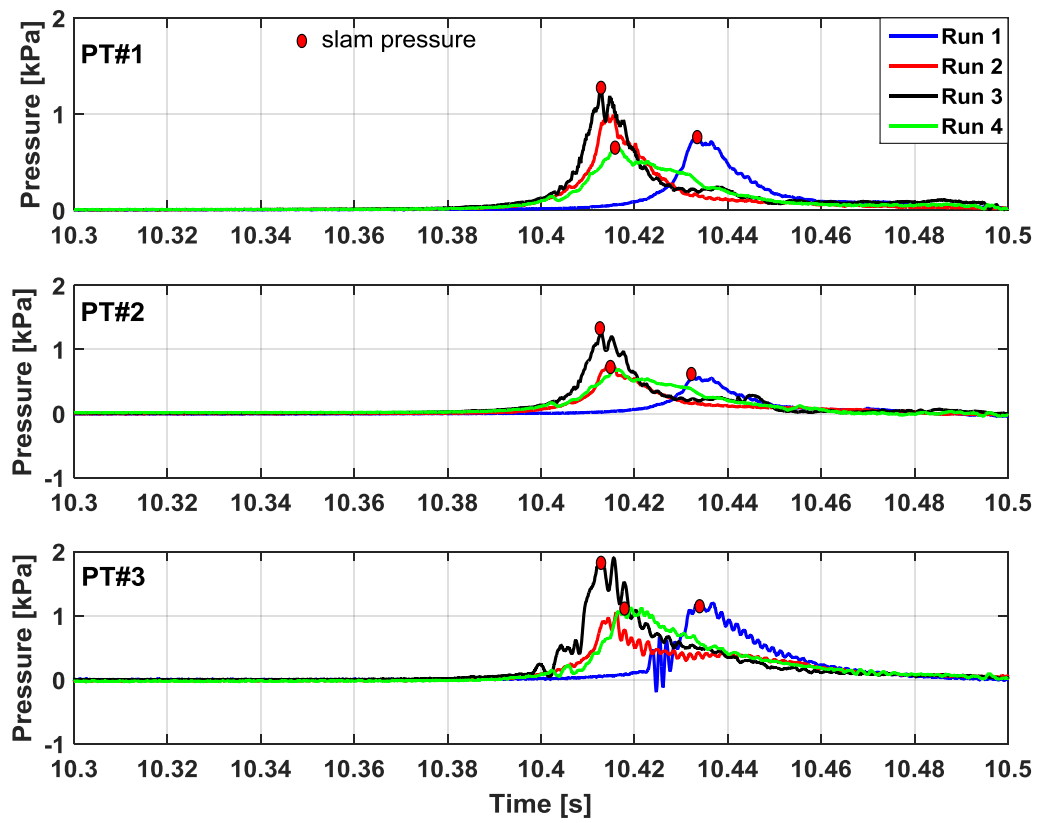


Figure 9. Resulting wave-in-deck pressures around the forward column (PT#1 – PT#3) using four repeated runs ($H_{\text{meas.}} = 219.60 \text{ mm}$, $T_{\text{meas.}} = 1.52 \text{ s}$).

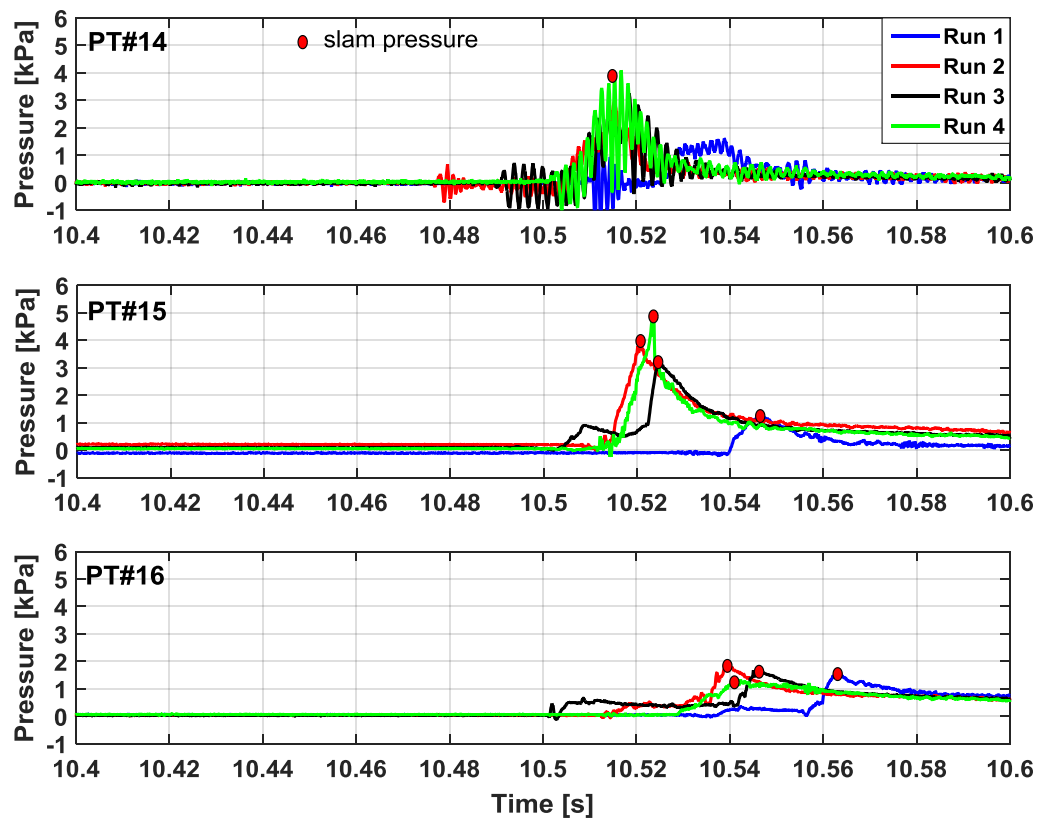


Figure 10. Resulting wave-in-deck pressures around the aft column (PT#14 – PT#16) using four repeated runs ($H_{\text{meas.}} = 219.60 \text{ mm}$, $T_{\text{meas.}} = 1.52 \text{ s}$).

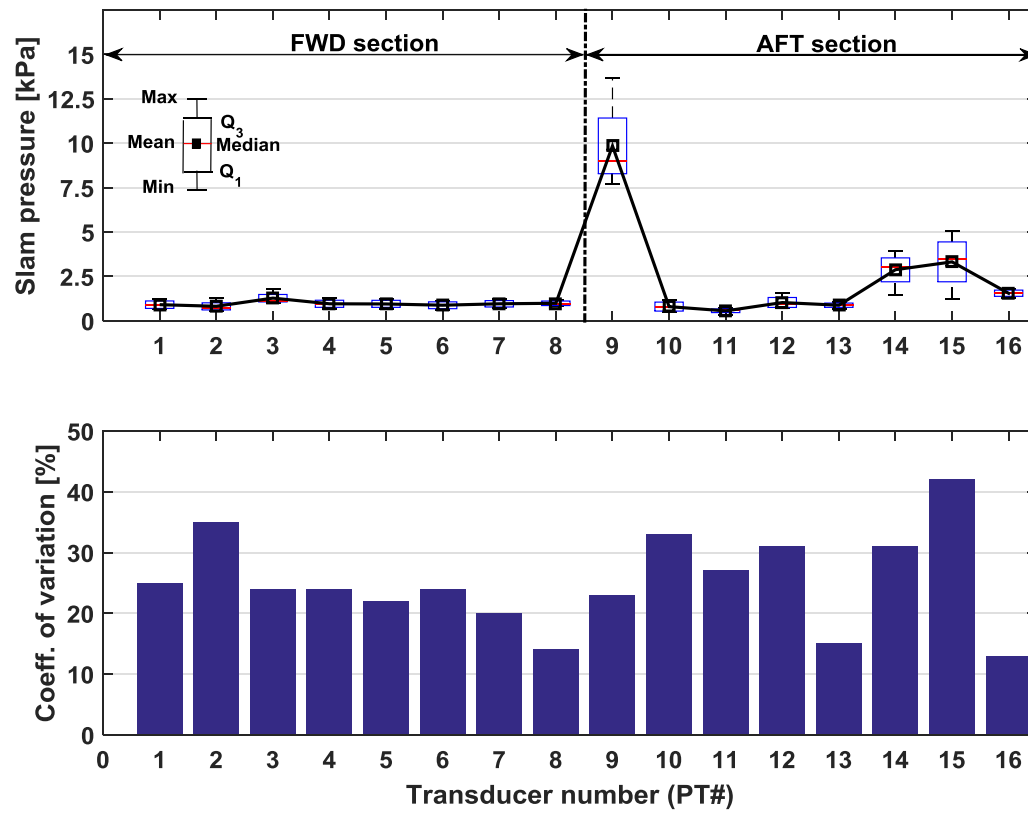


Figure 11. Variation of impact pressures measured by sixteen pressure transducers ($H_{\text{meas.}} = 218.8 \text{ mm}$, $T_{\text{meas.}} = 1.52 \text{ s}$): boxplots (top); coefficient of variation, CV (bottom).

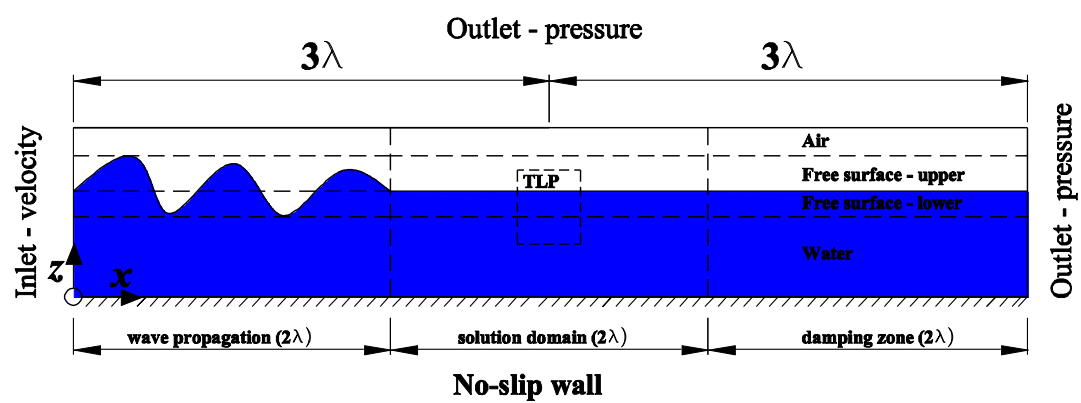


Figure 12. Numerical wave tank used in CFD simulations during wave generation without the model in-place.

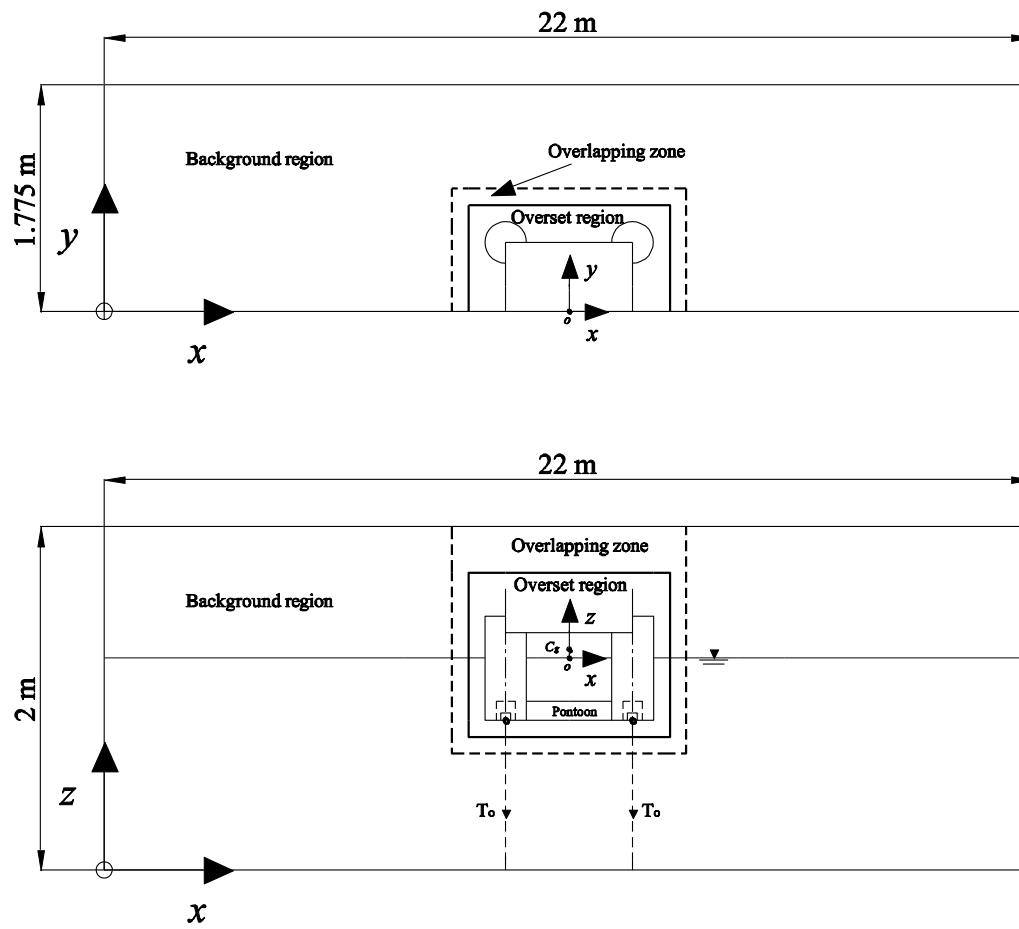


Figure 13. A sketch showing overlapping between background and overset regions: plan view (top); side view (bottom) [not to scale].

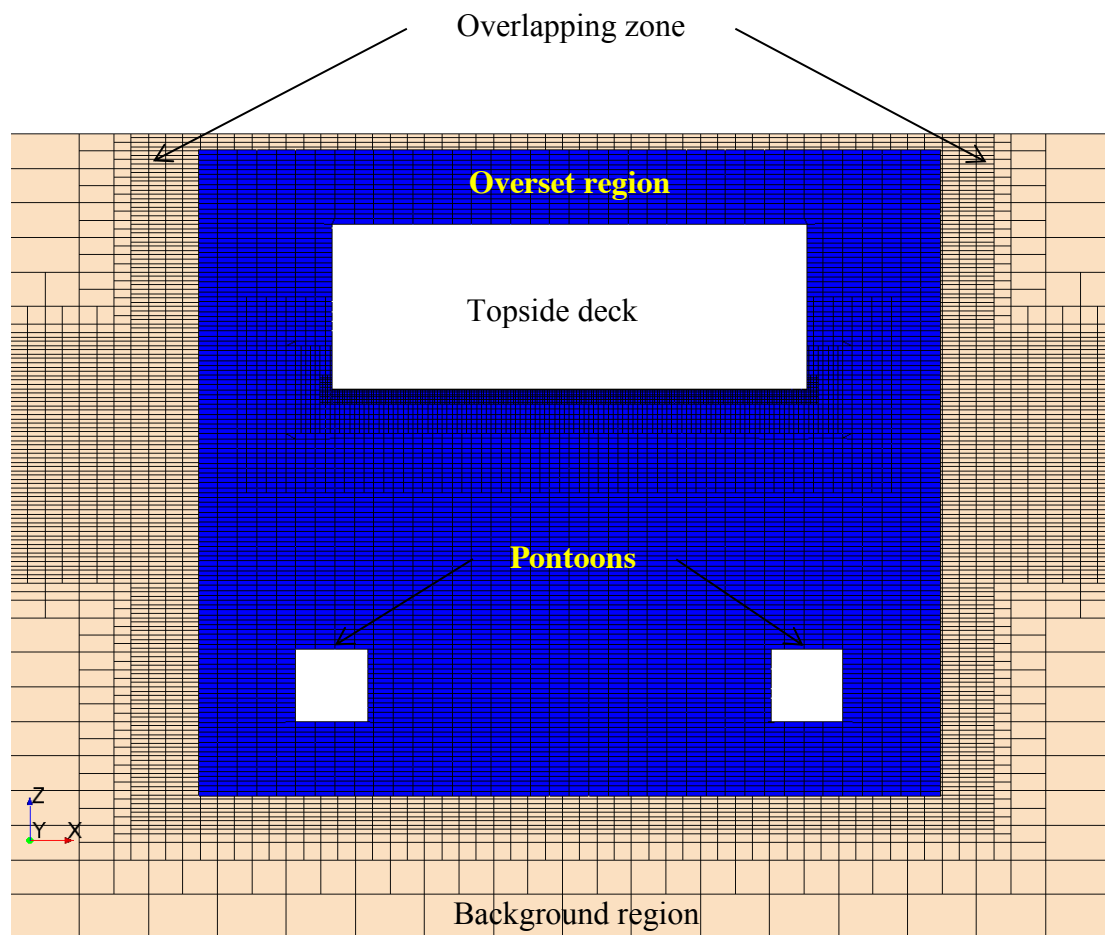


Figure 14. Snapshot at xz plane showing mesh distribution near the TLP model.

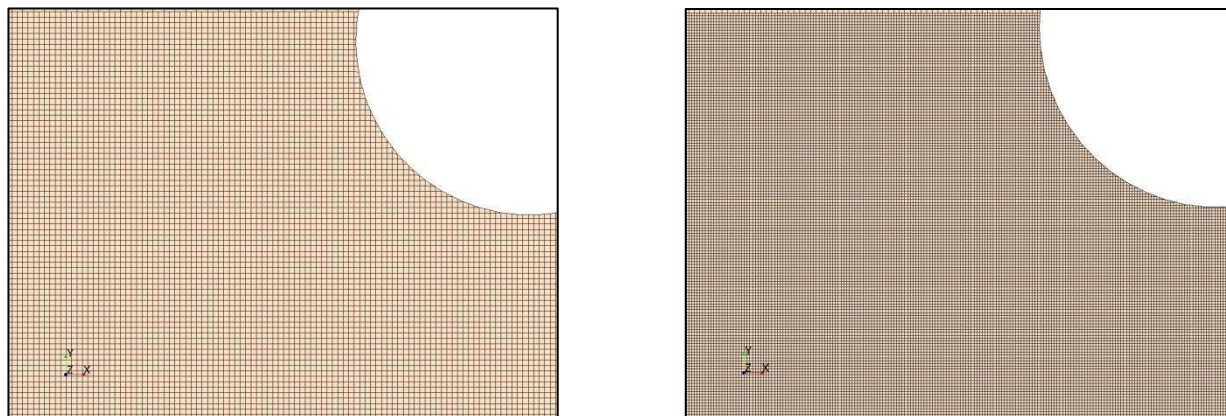


Figure 15. Snapshots showing local refinement of surface mesh at the deck underside near the aft column: reference mesh, level 1 (left); fine mesh, level 2 (right).

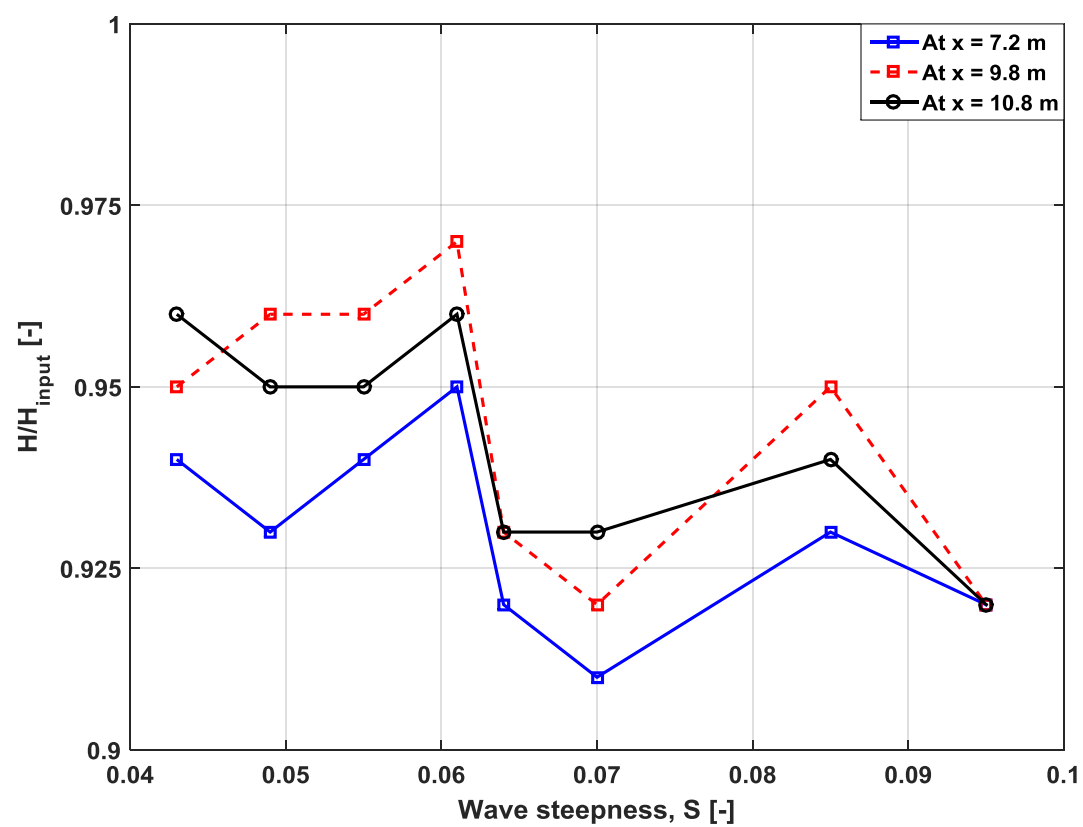


Figure 16. Results of wave height (H) predicted by CFD to H_{input} versus wave steepness at different locations along the computational domain. Mesh size: $\lambda/dx > 20$ and $H_{input}/dz > 80$.

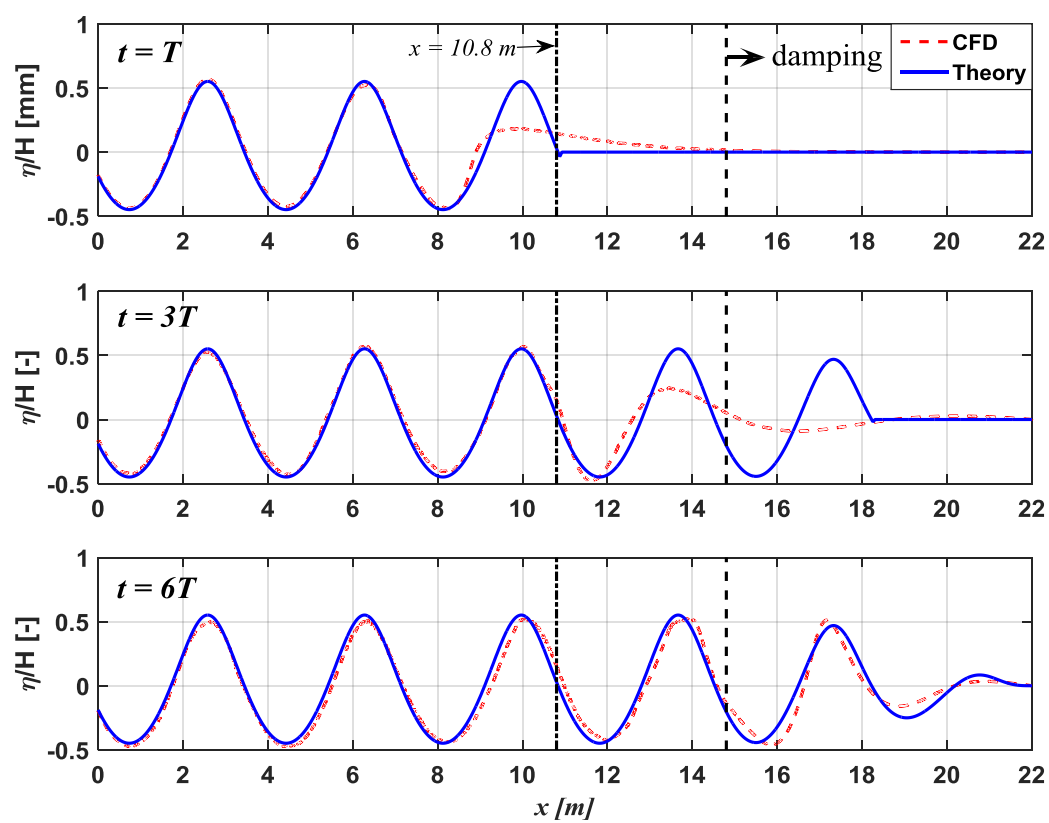


Figure 17. Comparisons between CFD and theoretical solutions of wave elevation along the computational domain for condition 3 ($H_{\text{input}} = 220$ mm, $T_{\text{input}} = 1.52$ s, $S = 0.061$): at time = one wave period (top); at time = three wave periods (middle); at time = six wave periods (bottom).

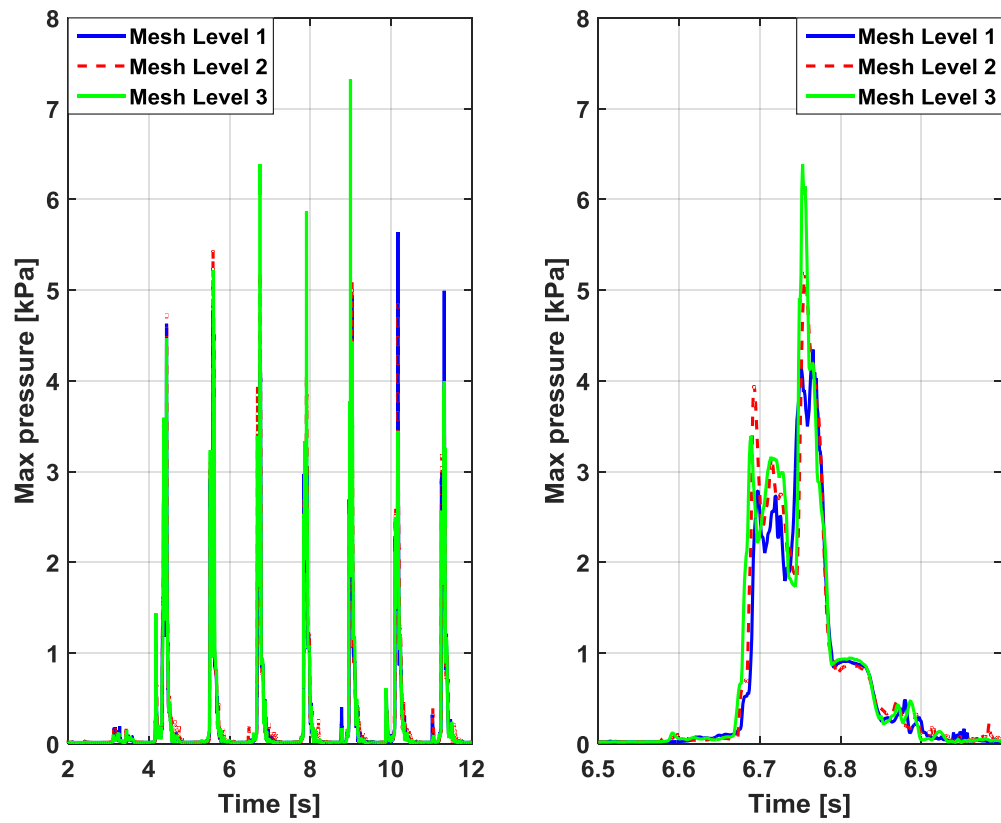


Figure 18. Results of sensitivity analysis of maximum pressure at the deck underside due to mesh density for condition 5 ($H_{input} = 201.6$ mm, $T_{input} = 1.163$ s, $S = 0.095$): time history of multiple wave-in-deck impact events (left); time history of a single wave-in-deck impact event (right).

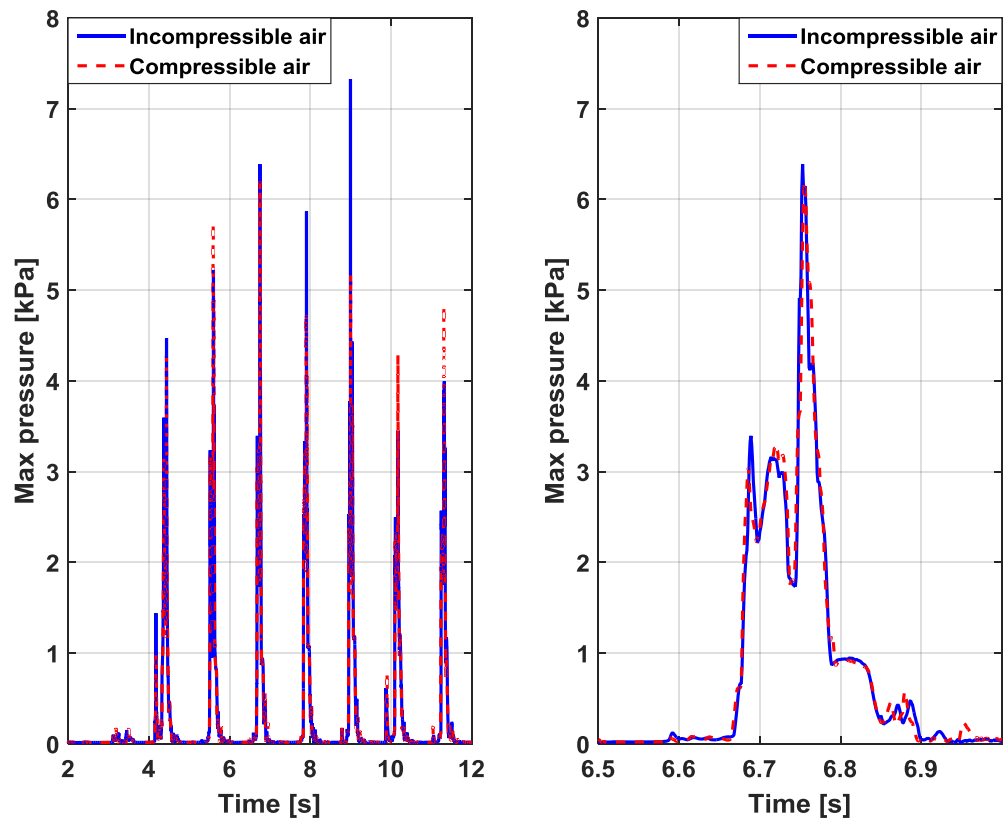


Figure 19. Results of sensitivity analysis of maximum pressure at the deck underside due to air compressibility using mesh level 3 for condition 5 ($H_{input} = 201.6$ mm, $T_{input} = 1.163$ s, $S = 0.095$): time history of multiple wave-in-deck impact events (left); time history of a single wave-in-deck impact event (right).

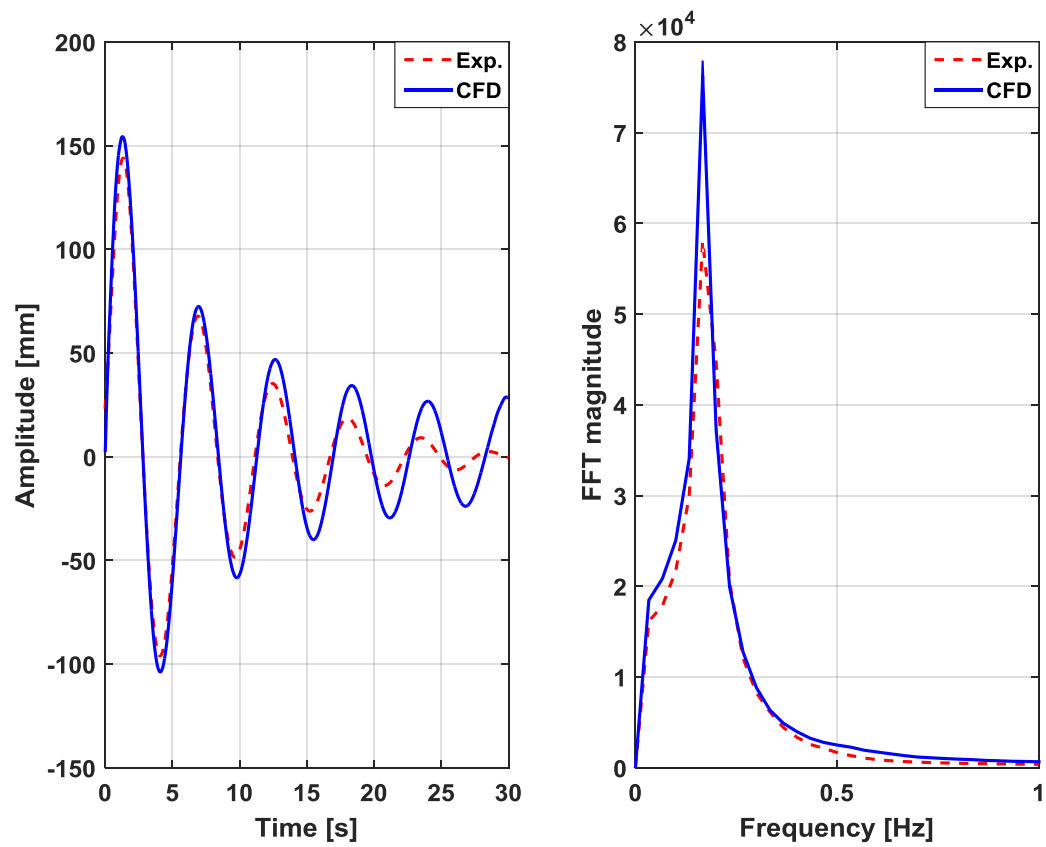


Figure 20. Free decay test results of CFD and experiments for surge motion: time history (left); FFT results (right).

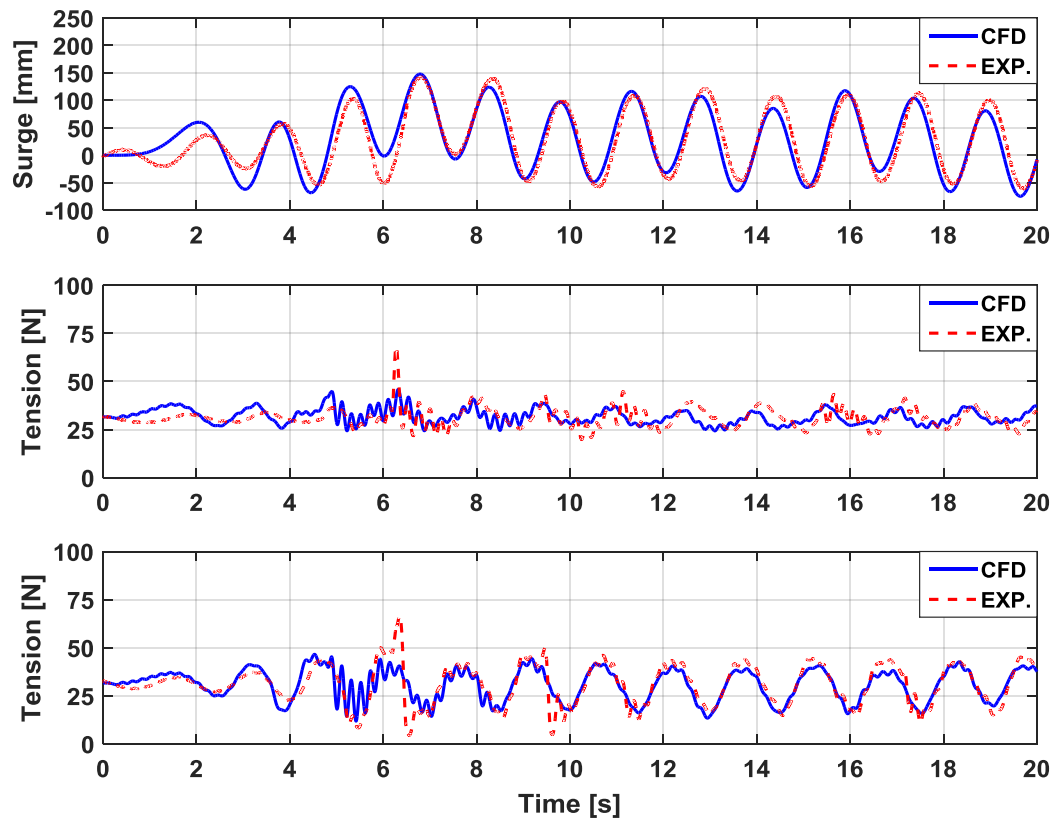


Figure 21. Comparison of CFD and experimental results for condition 2 ($H_{input} = 200$ mm, $T_{input} = 1.52$ s): surge motion (top); tension in the up-wave tendon (middle); tension in the down-wave tendon (bottom).

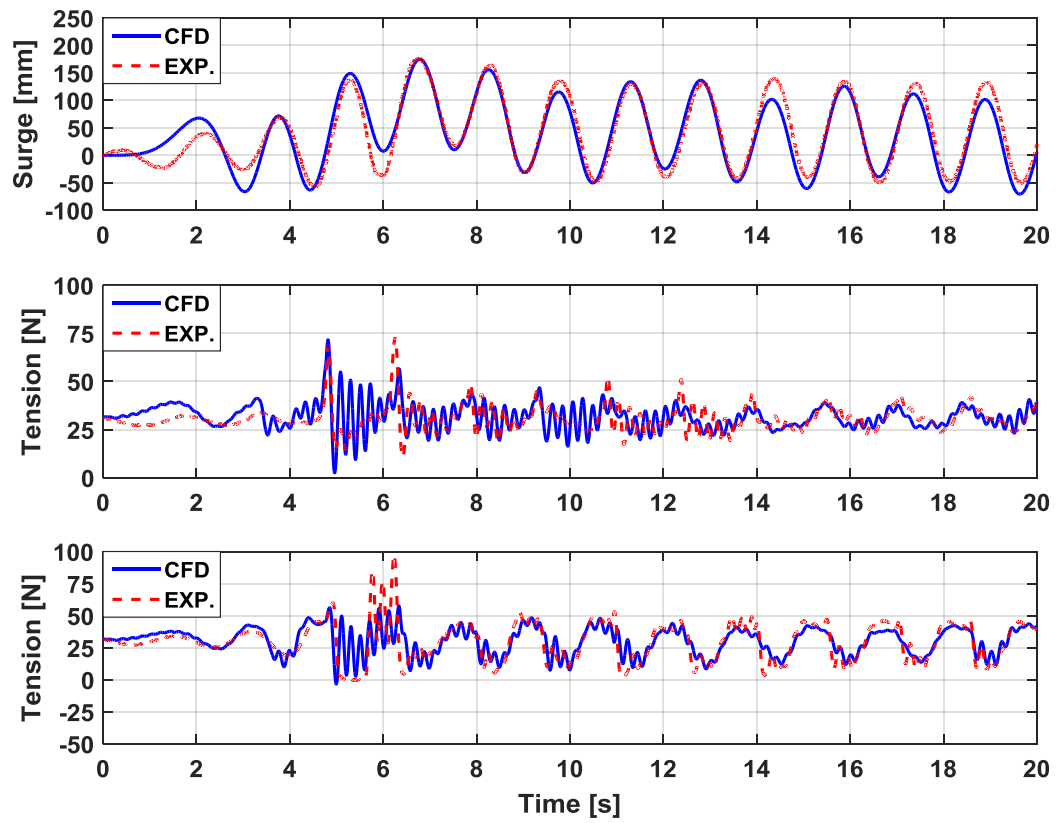


Figure 22. Comparison of CFD and experimental results for condition 3 ($H_{input} = 220$ mm, $T_{input} = 1.52$ s): surge motion (top); tension in the up-wave tendon (middle); tension in the down-wave tendon (bottom).

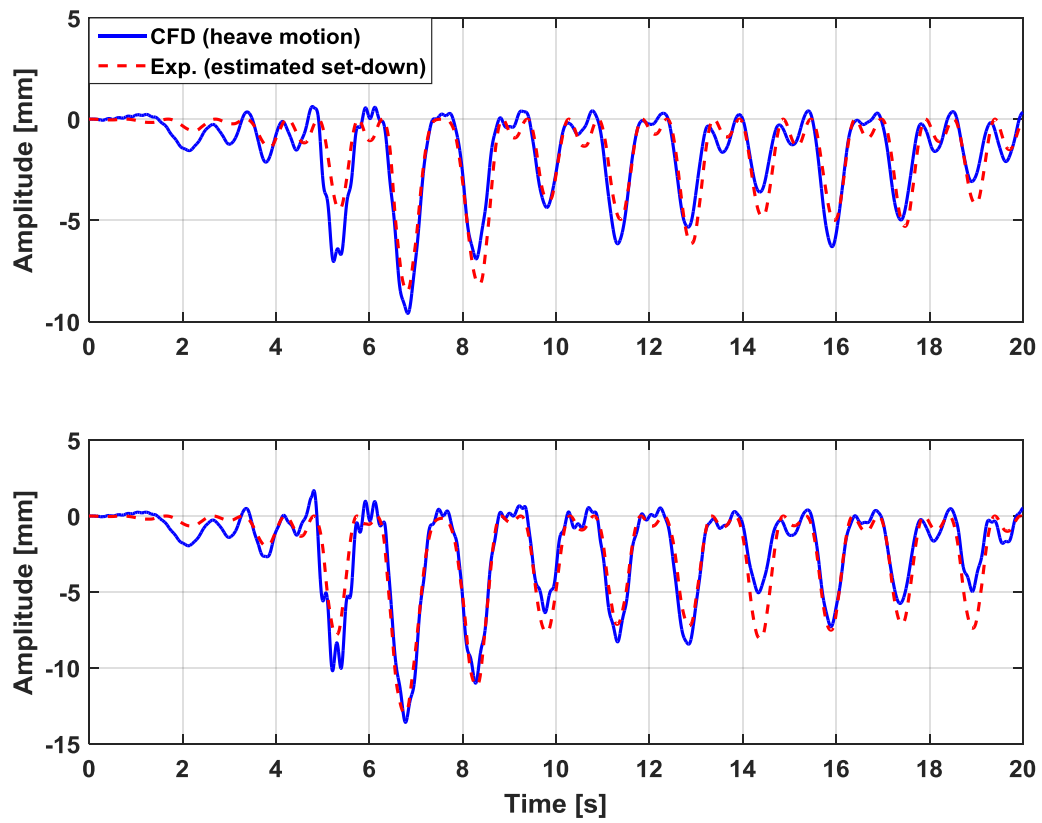


Figure 23. Time history of heave motion predicted by CFD and the estimated set-down by measurements: for condition 2 (top); for condition 3 (bottom).

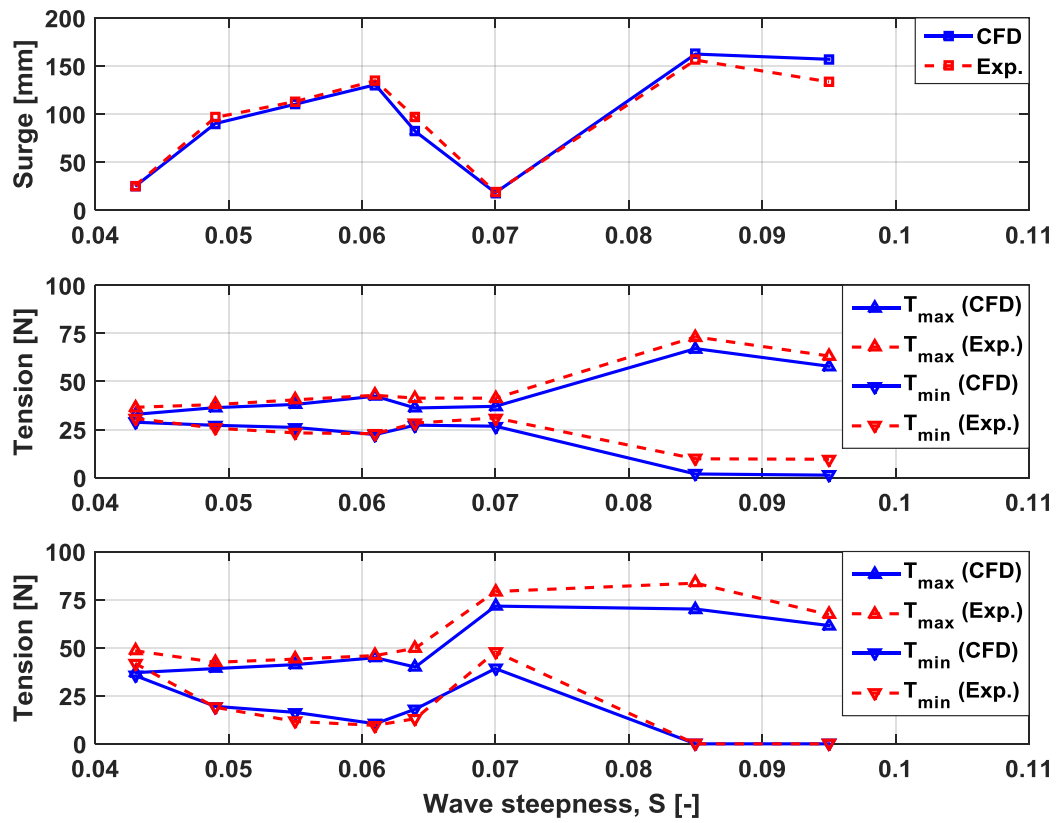


Figure 24. Comparison of CFD and experimental results: maximum amplitude of surge motion (top); maximum and minimum tension (T_{max} and T_{min}) in the up-wave tendon, Leg#1 (middle); maximum and minimum tension (T_{max} and T_{min}) in the down-wave tendon, Leg#4 (bottom).

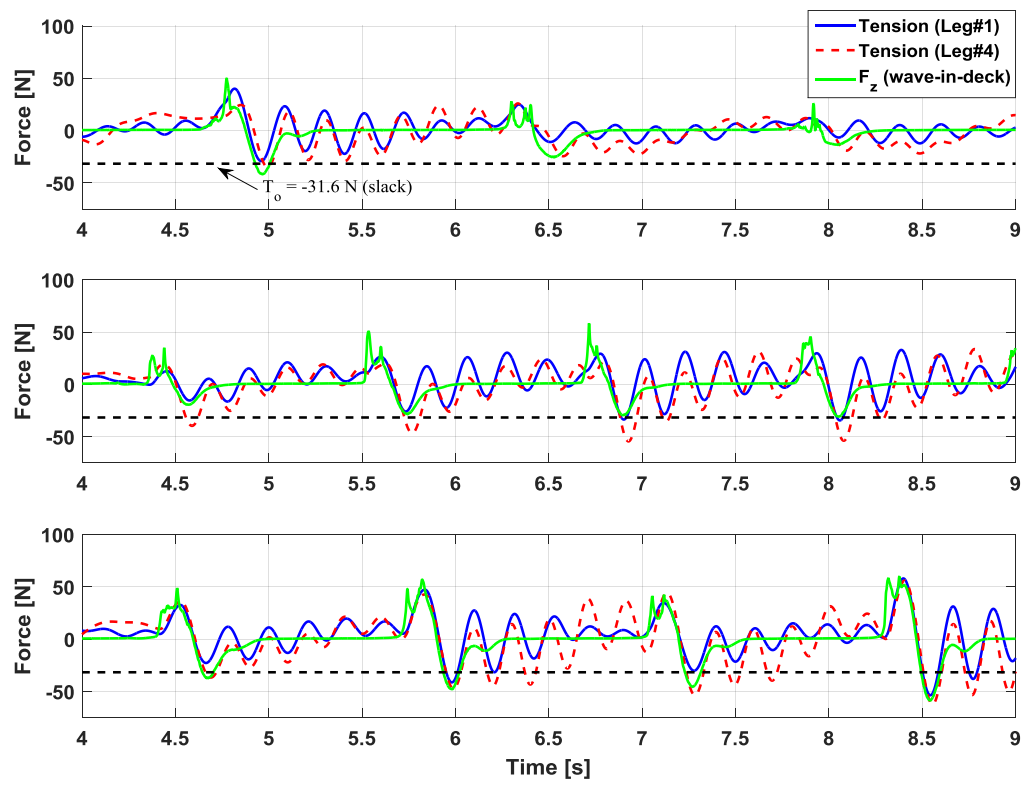


Figure 25. Time history of CFD results for tendon tensions in the up-wave and down-wave tendons and the simultaneous vertical wave-in-deck force, F_z ; for condition 3 (top); for condition 5 (middle); for condition 8 (bottom).

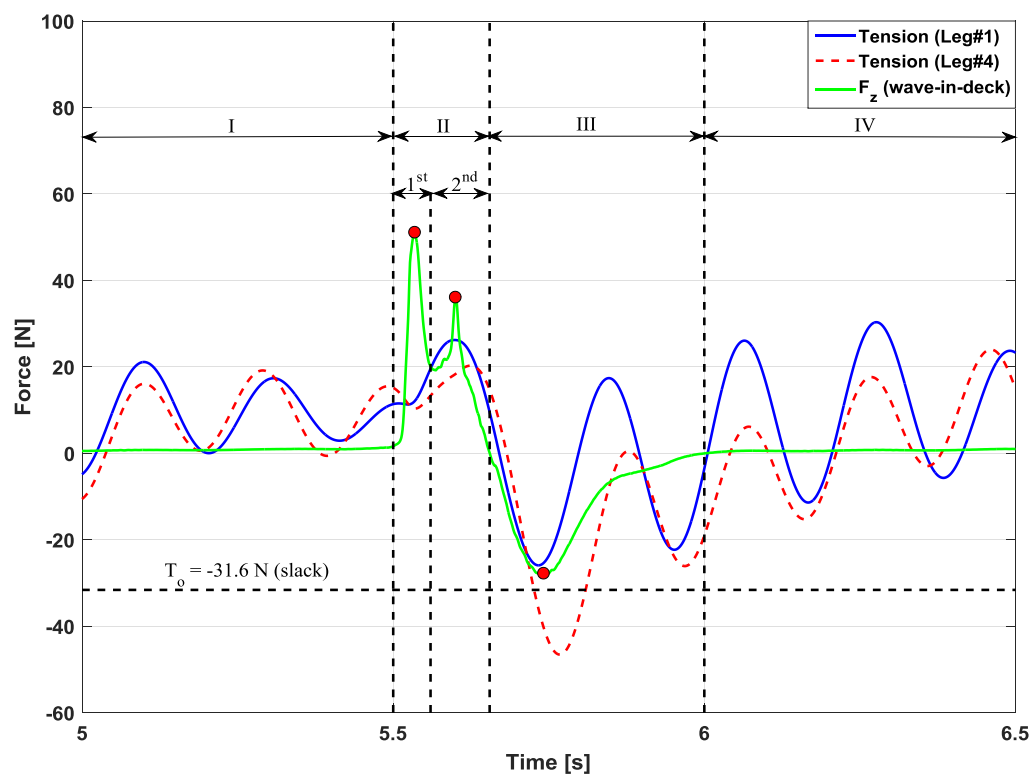


Figure 26. Time history of CFD results for a single wave-in-deck event and the associated tendon tensions in the up-wave and down-wave tendons for condition 5: $H_{input} = 201.6$ mm, $T_{input} = 1.163$ s.

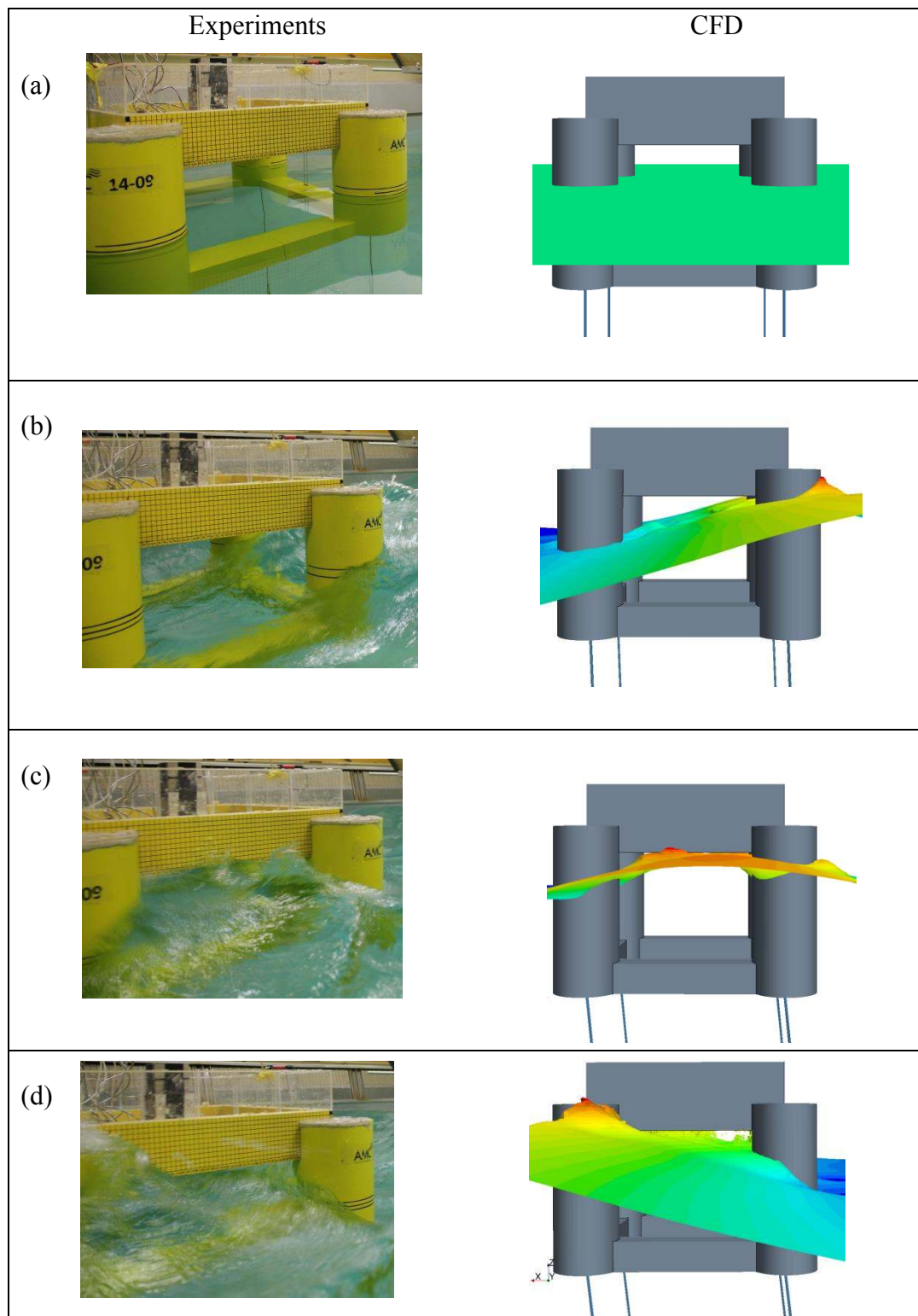


Figure 27. Snapshots at different time instances showing an extreme wave impact on the TLP model at the towing tank (left) and using CFD simulations (right): (a) no wave (still-water) condition; (b) wave run-up on the forward columns; (c) wave impact on the deck underside; (d) wave impact on the aft section of deck underside and water overtopping on the aft columns. Condition 5 ($H_{input} = 201.6$ mm, $T_{input} = 1.163$ s).

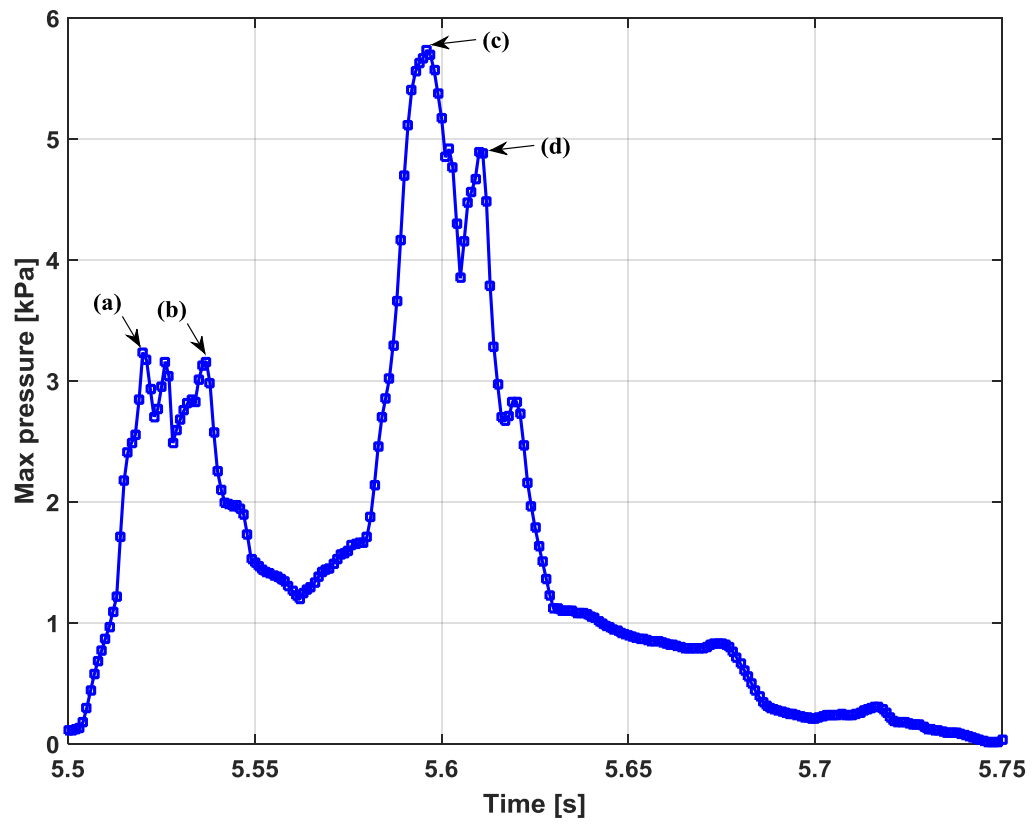


Figure 28. Time history of maximum pressure at the deck underside computed using mesh level 3 with compressible air for condition 5 ($H_{input} = 201.6$ mm, $T_{input} = 1.163$ s).

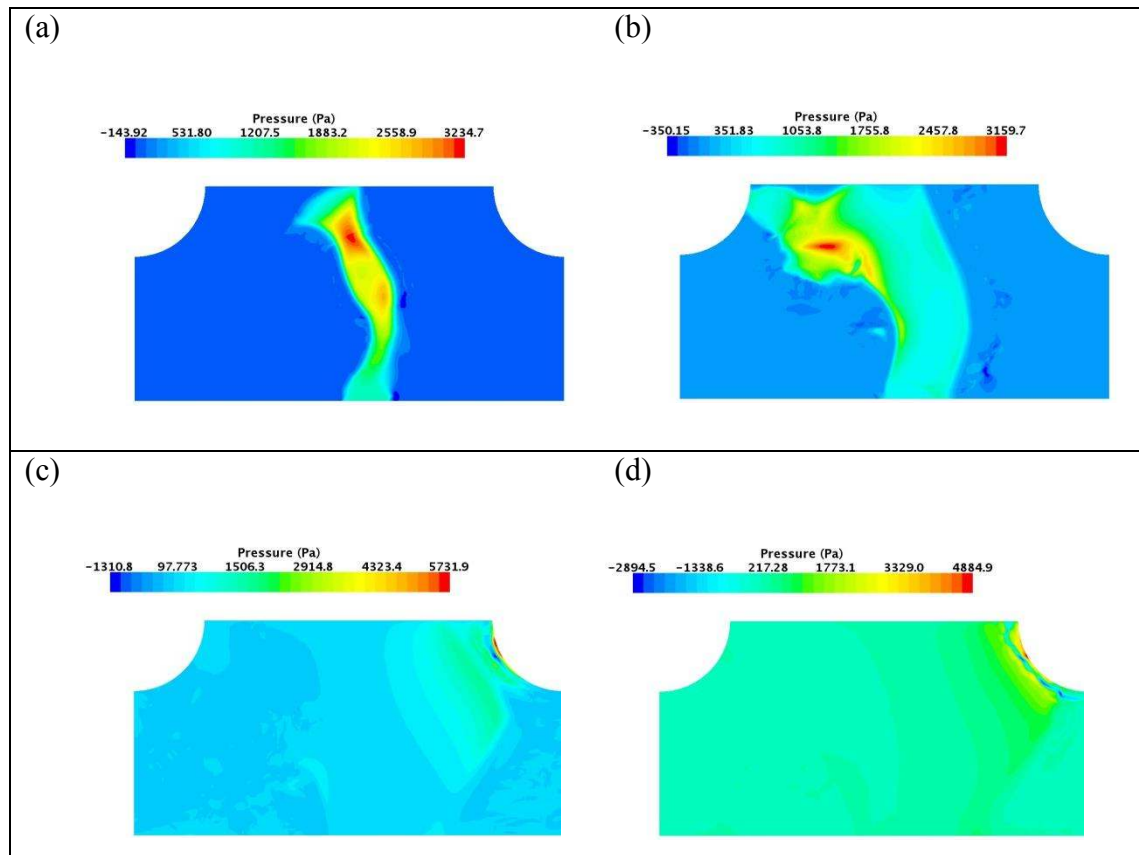


Figure 29. Pressure contours for condition 5 ($H_{\text{input}} = 201.6 \text{ mm}$, $T_{\text{input}} = 1.163 \text{ s}$) using mesh level 3 and compressible air. Time instances (a) – (d) are shown in Figure 28.

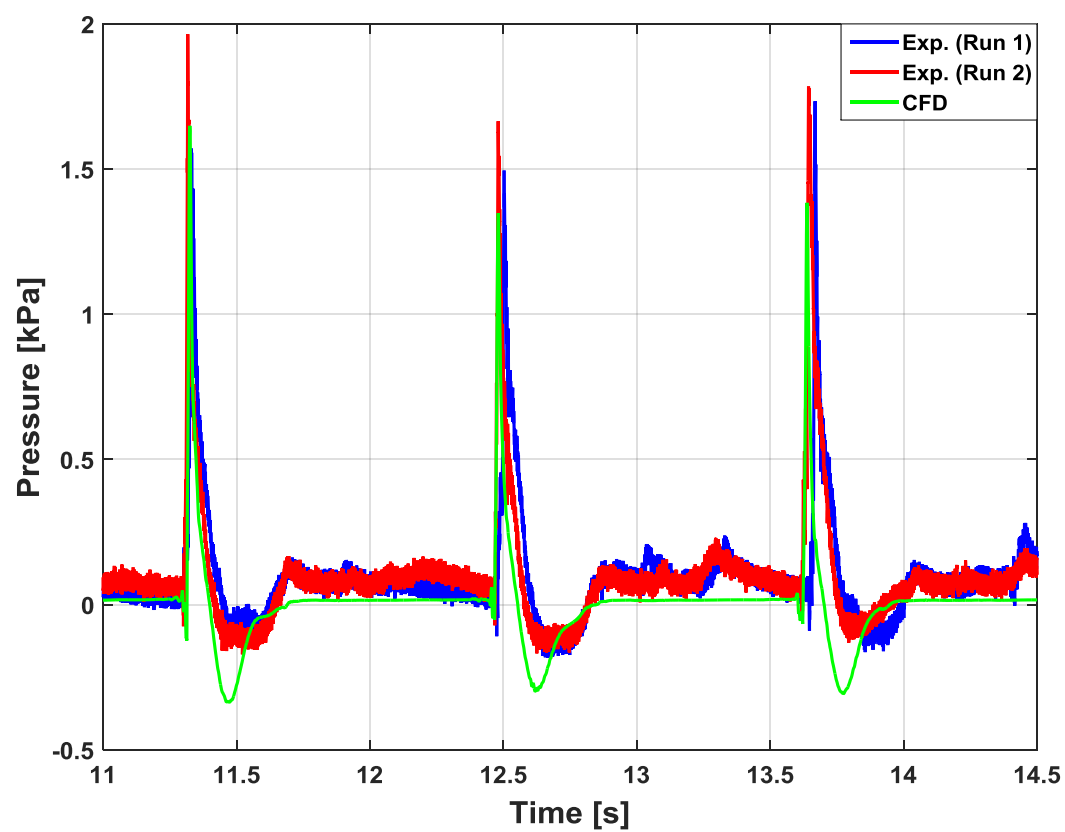


Figure 30. Time history of wave-in-deck pressure at PT#16 obtained by experiments and CFD for Condition 5 ($H_{\text{input}} = 201.6$ mm, $T_{\text{input}} = 1.163$ s).